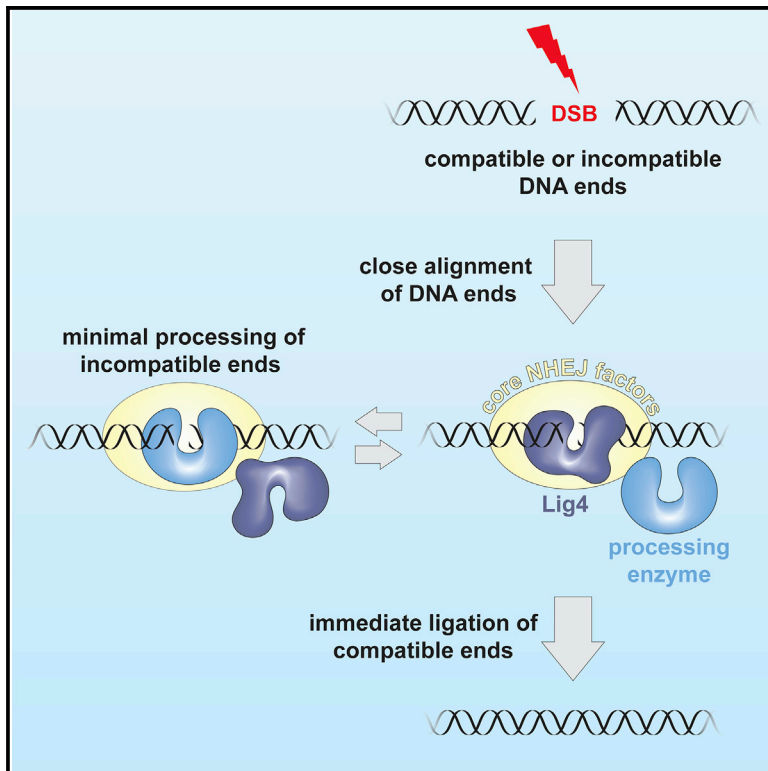


Molecular Cell

A Mechanism to Minimize Errors during Non-homologous End Joining

Graphical Abstract



Authors

Benjamin M. Stinson,
Andrew T. Moreno,
Johannes C. Walter, Joseph J. Loparo

Correspondence

johannes_walter@hms.harvard.edu
(J.C.W.),
joseph_loparo@hms.harvard.edu (J.J.L.)

In Brief

Stinson et al. demonstrate that DNA end processing during non-homologous end joining (NHEJ) occurs only after DNA ends are aligned for ligation. This mechanism minimizes errors during NHEJ and helps maintain genome stability.

Highlights

- *Xenopus* egg extracts efficiently recapitulate DNA end processing during NHEJ
- Compatible DNA ends are not processed; incompatible ends are minimally processed
- Ends are processed in a ligation-competent complex and otherwise protected
- Coordinating end processing with ligation minimizes errors during NHEJ

A Mechanism to Minimize Errors during Non-homologous End Joining

Benjamin M. Stinson,¹ Andrew T. Moreno,¹ Johannes C. Walter,^{1,2,*} and Joseph J. Loparo^{1,3,*}

¹Department of Biological Chemistry and Molecular Pharmacology, Harvard Medical School, Boston, MA 02115, USA

²Howard Hughes Medical Institute, Boston, MA 02115, USA

³Lead Contact

*Correspondence: johannes_walter@hms.harvard.edu (J.C.W.), joseph_loparo@hms.harvard.edu (J.J.L.)

<https://doi.org/10.1016/j.molcel.2019.11.018>

SUMMARY

Enzymatic processing of DNA underlies all DNA repair, yet inappropriate DNA processing must be avoided. In vertebrates, double-strand breaks are repaired predominantly by non-homologous end joining (NHEJ), which directly ligates DNA ends. NHEJ has the potential to be highly mutagenic because it uses DNA polymerases, nucleases, and other enzymes that modify incompatible DNA ends to allow their ligation. Using frog egg extracts that recapitulate NHEJ, we show that end processing requires the formation of a “short-range synaptic complex” in which DNA ends are closely aligned in a ligation-competent state. Furthermore, single-molecule imaging directly demonstrates that processing occurs within the short-range complex. This confinement of end processing to a ligation-competent complex ensures that DNA ends undergo ligation as soon as they become compatible, thereby minimizing mutagenesis. Our results illustrate how the coordination of enzymatic catalysis with higher-order structural organization of substrate maximizes the fidelity of DNA repair.

INTRODUCTION

Genome stability is central to the survival of all organisms. Faithful DNA replication and repair ensure genome stability, yet these processes use scores of enzymes that chemically alter DNA and must be carefully regulated. A prominent example is non-homologous end joining (NHEJ), which repairs the majority of DNA double-strand breaks (DSBs) in vertebrate cells through direct re-ligation (Chiruvella et al., 2013; Karanam et al., 2012; Lieber, 2010; Radhakrishnan et al., 2014; Waters et al., 2014a). DSBs arise from myriad spontaneous (e.g., reactive oxygen species, ionizing radiation) and programmed (e.g., V(D)J recombination, Cas9) sources, and failure to repair such DSBs results in cell death or malignancy-driving genomic rearrangements (Aparicio et al., 2014). Broken DNA ends are chemically diverse, and many are not compatible for immediate ligation. To solve this problem, NHEJ end-processing enzymes modify DNA ends until

they are ligatable (Povirk, 2012). However, end processing has the potential to introduce mutations by inserting or deleting nucleotides. Whereas this mutagenicity is exploited for immunoglobulin and T cell receptor gene diversification and CRISPR-Cas9 gene disruption, it needs to be restrained during the repair of unprogrammed breaks to prevent genome instability. At present, little is known about how DNA processing during NHEJ is regulated.

NHEJ is initiated by the ring-shaped Ku70/Ku80 heterodimer (Ku) (Mimori et al., 1986; Walker et al., 2001), which encircles broken DNA ends and recruits the DNA-dependent protein kinase catalytic subunit (DNA-PKcs) (Falck et al., 2005; Gottlieb and Jackson, 1993; Lees-Miller et al., 1990; Sibanda et al., 2017). DNA-PKcs phosphorylates multiple NHEJ factors, including itself, and its kinase activity is required for efficient end joining (Davis et al., 2014; Dobbs et al., 2010; Jette and Lees-Miller, 2015). Ends are ligated by a complex of DNA ligase IV (Lig4) and XRCC4 (Grawunder et al., 1997), and joining is stimulated by the XRCC4 paralog XLF (Ahnesorg et al., 2006). Another XRCC4-like protein, PAXX (paralog of XLF and XRCC4), appears to have functions overlapping with those of XLF (Kumar et al., 2016; Ochi et al., 2015; Tadi et al., 2016; Xing et al., 2015). These core factors cooperate with end-processing enzymes to allow the joining of chemically incompatible ends: DNA polymerases (e.g., pol λ , pol μ) fill in overhangs and gaps (Bertocci et al., 2003, 2006; Lee et al., 2004; Ma et al., 2004; Mahajan et al., 2002), nucleases (e.g., Artemis) remove damaged nucleotides (Ma et al., 2002), polynucleotide kinase 3'-phosphatase (PNKP) adds 5'-phosphates and removes 3' phosphates (Koch et al., 2004), tyrosyl-DNA phosphodiesterase 1 (Tdp1) removes topoisomerase I adducts (Yang et al., 1996) and other 3' modifications (Inamdar et al., 2002; Interthal et al., 2005), Tdp2 removes 5' DNA-topoisomerase II adducts (Gómez-Herreros et al., 2013; Cortes Ledesma et al., 2009), and aprataxin removes 5' adenylate moieties resulting from abortive ligation (Ahel et al., 2006; Clements et al., 2004). Thus, processing enzymes equip NHEJ with numerous means to resolve end incompatibility.

NHEJ processing enzymes can introduce unnecessary mutations, leading to the widespread notion that NHEJ is highly error prone and “sloppy.” For example, the overexpression of site-specific endonucleases in mammalian cells leads to the formation of NHEJ-dependent junctions with variable sequences (Lin et al., 1999; Lukacsovich et al., 1994; Phillips and Morgan, 1994; Rouet et al., 1994; Sargent et al., 1997). However, multiple

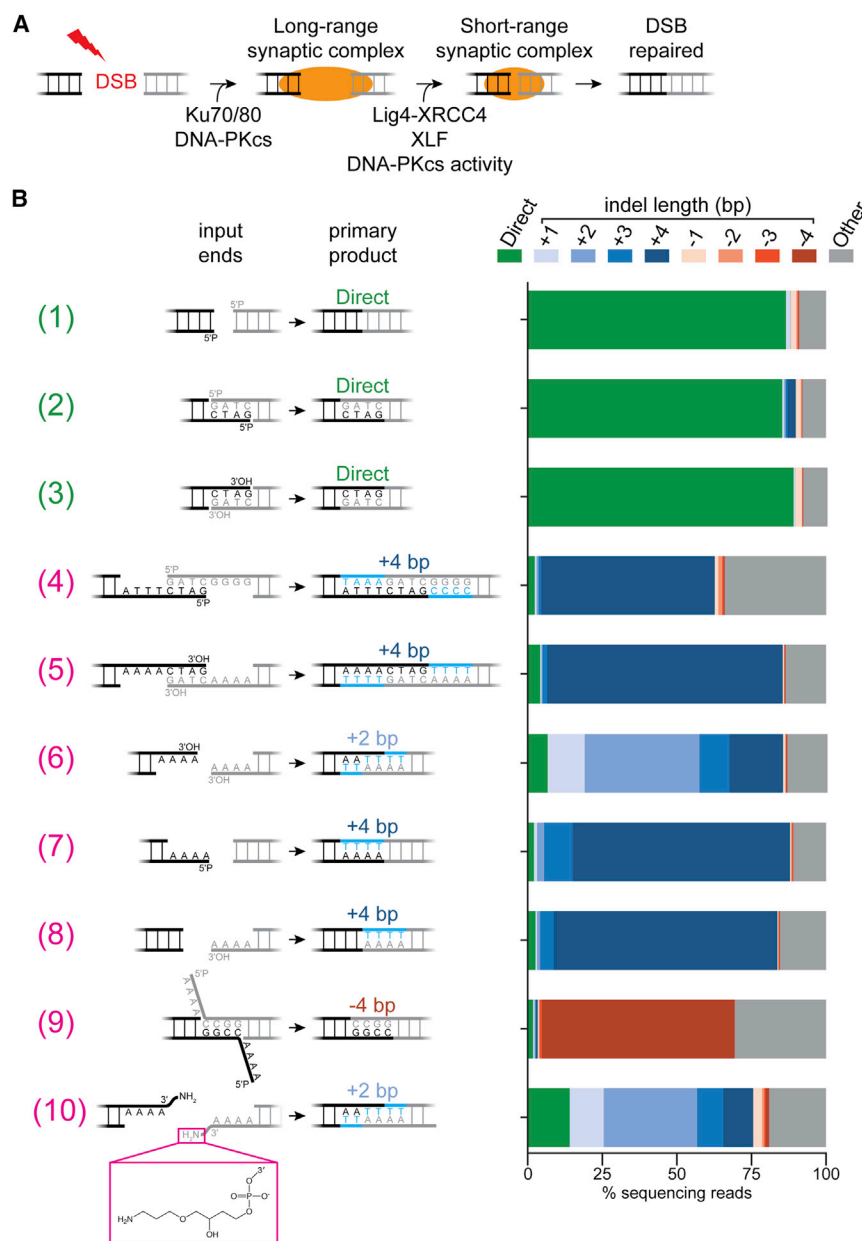


Figure 1. Joining of Diverse End Structures in *Xenopus* Egg Extracts

(A) Model of two-stage DNA-end synapsis during NHEJ (Graham et al., 2016).

(B) Linear DNA molecules with the indicated ends were added to egg extracts and incubated for 90 min. DNA was extracted, and joints were amplified by PCR and analyzed by paired-end Illumina sequencing. Indel length is relative to the direct ligation of the top strand depicted for each end pair. The light blue sequence corresponds to nucleotides inserted during joining. The bar graphs were generated by identifying junction reads with the indicated indel length and normalizing to the total number of reads. See [Method Details](#) for controls regarding the fidelity of amplification, library preparation, and sequencing. Analysis of aligned sequencing reads is reported in [Data S1](#).

rounds of cutting and accurate repair usually occur before an error arises. Consequently, the fidelity of repair is actually much higher than suggested by these studies. When re-cleavage is disfavored or disallowed, compatible (i.e., blunt, complementary) ends are usually repaired without errors (Baumann and West, 1998; Bétermier et al., 2014; Feldmann et al., 2000; Lin et al., 2013). Moreover, the processing of incompatible ends is limited to the minimum required for ligation (Bétermier et al., 2014; Budman and Chu, 2005; Guirouilh-Barbat et al., 2004; Waters et al., 2014b). These studies suggest that NHEJ minimizes the extent of end processing and prioritizes ligation, but the molecular basis of this prioritization is unknown.

The coordination of end processing with synapsis, which aligns DNA ends for ligation, may play an important regulatory

role. Using single-molecule Förster resonance energy transfer (smFRET) imaging, we previously showed that synapsis occurs in two stages (Figure 1A; Graham et al., 2016): initially, Ku and DNA-PKcs form a “long-range” synaptic complex, in which dye-labeled DNA ends are tethered at a distance greater than that required to observe FRET (>100 Å); subsequently, DNA-PKcs kinase activity, XLF, and Lig4-XRCC4 convert the long-range complex into a high FRET “short-range” complex in which ends are held close together in a ligation-competent state. Stable synapsis of DNA ends using purified human proteins shows similar requirements (Wang et al., 2018). Conflicting models have been proposed in which end processing occurs independently of synapsis (Lieber, 2010; Ma et al., 2004), while ends are synapsed (Conlin et al., 2017; Waters et al., 2014b), or upon the dissolution of synapsis after failed ligation (Reid et al., 2017). However, without a means to simultaneously measure end synapsis and processing, distinguishing among these models has been impossible.

Here, we use single-molecule fluorescence imaging in *Xenopus* egg extracts to observe DNA-end synapsis and processing in real time. We first establish that egg extracts support the ligation of chemically diverse DNA ends and that the joining of each type of incompatible DNA end requires a distinct processing enzyme. Second, we show that the activities of all of the processing enzymes examined require Lig4-XRCC4, XLF, and DNA-PKcs kinase activity, establishing a dependence on processing on the formation of the short-range synaptic complex. Moreover, smFRET assays that simultaneously monitor synapsis and end processing demonstrate that processing occurs preferentially in the short-range synaptic complex. Our

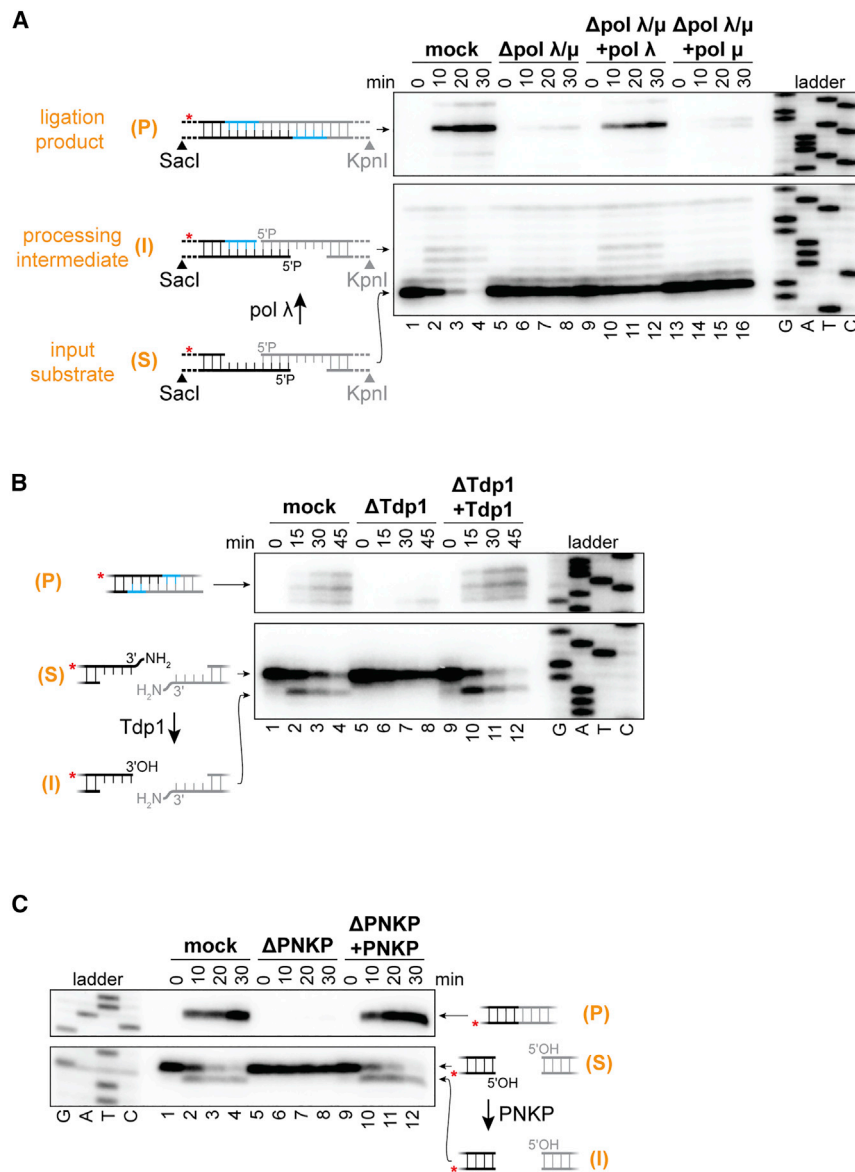


Figure 2. Involvement of Pol λ and Tdp1 in End Processing

(A–C) Radiolabeled linear DNA molecules were added to the indicated egg extracts, and reaction samples were stopped at the indicated time points. Panels differ by input DNA ends, depicted at right. DNA was extracted, digested, and analyzed by denaturing PAGE and autoradiography. Bottom panels: unjoined DNA ends; top panels: joined DNA ends. The red asterisk indicates a radiolabeled strand. The immunodepletion of pol λ alone blocked the joining of the ends depicted in (A) (see Figure S1H, lanes 22–24). The immunodepleted extracts were supplemented with the following final concentrations of recombinant protein as indicated: pol λ and pol μ, 10 nM; Tdp1, 40 nM. I, processing intermediate; P, ligation product; S, input substrate. Top panels depict “head-to-tail” joints (see Figure S1B). “Head-to-head” joints show similar products and are shown in Figures S1C, S1E, and S1F.

added these substrates to egg extracts, and sequenced the resulting NHEJ repair junctions (Figures 1B and S1A). We verified that a representative product spectrum was maintained through amplification and sample processing (see Method Details). Compatible ends (i.e., blunt, complementary) were typically ligated without processing (Figure 1B, 1–3), underscoring that NHEJ is not intrinsically mutagenic. Due to minor contaminants in the input DNA and errors introduced during sample preparation, these measurements represent a lower limit of NHEJ fidelity (see Method Details). Incompatible ends underwent a variety of processing events before joining, including gap filling (Figure 1B, 4–8), nucleolytic trimming (Figure 1B, 9), and 3' adduct removal (Figure 1B, 10). The extent of processing was generally limited

results establish a model in which confining end processing to the Lig4-dependent short-range synaptic complex promotes the immediate ligation of compatible ends and ensures that incompatible ends are ligated as soon as they become compatible, thereby minimizing end processing.

RESULTS

Egg Extracts Recapitulate Diverse End-Processing Events

To investigate the regulation of processing, we used *Xenopus laevis* egg extracts, which join DNA ends in a manner dependent on Ku, DNA-PKcs, Lig4-XRCC4, and XLF (Graham et al., 2016; Labhart, 1999; Pfeiffer and Vielmetter, 1988; Thode et al., 1990; Di Virgilio and Gautier, 2005). We generated a series of linear DNA substrates with compatible or incompatible ends,

to a few nucleotides, and most of the substrates were joined with a single predominant sequence, even in the absence of microhomology to guide end alignment.

To identify end-processing enzymes in this cell-free system, we added linear DNA substrates containing radioactively labeled DNA ends (Figure S1A) to egg extract that had been immunodepleted of specific factors. At different time points, the DNA was recovered, digested with SacI and KpnI, separated by denaturing PAGE, and the starting material, processing intermediates, and ligation products were visualized at nucleotide resolution by autoradiography (Figure 2A). Immunodepletion of pol λ and pol μ prevented gap filling of DNA ends with paired primer termini (Figures 2A, lanes 1–8, and S1C). Re-addition of recombinant pol λ but not pol μ restored efficient gap filling and ligation of these DNA ends (Figure 2A, lanes 9–16), consistent with previous reports (Nick McElhinny et al., 2005). Immunodepletion of

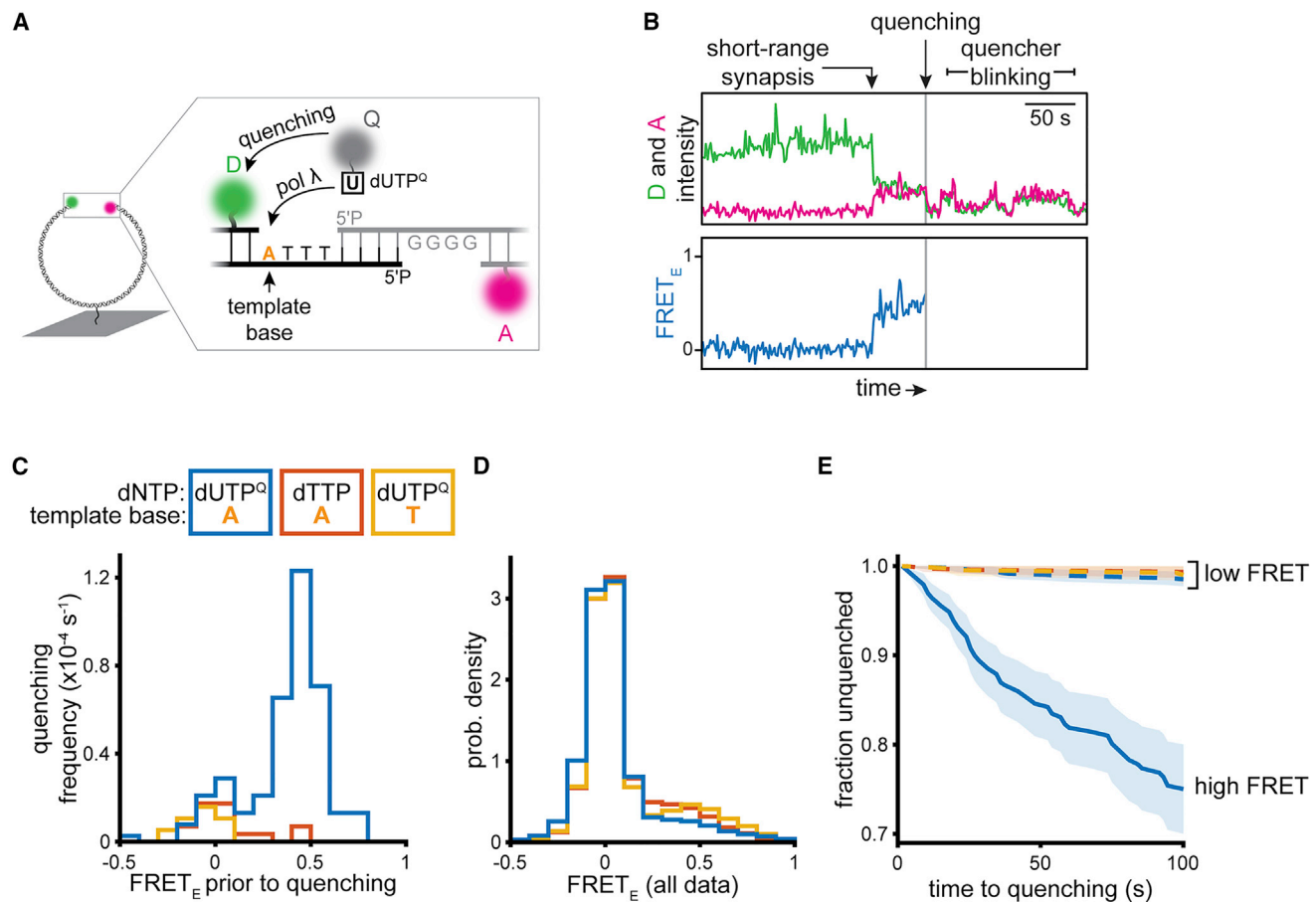


Figure 4. Pol λ Acts within the Short-Range Synaptic Complex

(A) Experimental scheme for the single-molecule assay of DNA-end synopsis and polymerase activity. A, Cy5 acceptor fluorophore; D, Cy3 donor fluorophore; Q, BHQ10 quencher. Fluorophore positions are noted in Table S1.

(B) Example trajectory. The Cy3 donor fluorophore was excited, and donor emission (green) and Cy5 acceptor emission (magenta) were recorded (top panel) and used to calculate FRET efficiency (blue, bottom panel). Scale bar, 50 s.

(C) Frequency of quenching events as a function of FRET efficiency immediately before quenching under the indicated conditions. Blue, extracts supplemented with dUTP^Q, adenine DNA template base (see A) substrate ($n = 145$ events from 9 independent experiments); red, extracts supplemented with dTTP, adenine DNA template base substrate ($n = 16$ events from 6 independent experiments); yellow, extracts supplemented with dUTP^Q, thymine DNA template base ($n = 8$ events from 6 independent experiments). See Method Details for the calculation of the quenching frequency and Figure S4A for the kinetic analysis and histograms represented as probability density.

(D) Histogram of the FRET efficiency of all frames for all molecules before censoring. Colors as in (C).

(E) Quenching survival kinetics (Kaplan-Meier estimate) under the indicated conditions (colors as in C). The x axis indicates dwell time in the high FRET (solid line) or low FRET (dashed lines) state before quenching. Shaded areas, 95% confidence intervals.

fluorophore near one DNA end and an acceptor fluorophore near the other end (Graham et al., 2016), which did not affect joining (Figure S3A). The extract was desalted and supplemented with deoxyuridine triphosphate (dUTP) labeled with the dark quencher BHQ-10 (dUTP^Q; Figure S3B) so that dUTP^Q incorporation opposite a templating adenosine would quench donor fluorescence (Figure 4A). dATP, deoxyguanosine triphosphate (dGTP), deoxycytidine triphosphate (dCTP), and ATP were also added to the desalted extract to support gap filling and joining. Ensemble experiments demonstrated that dUTP^Q was efficiently incorporated during the joining of these ends (Figure S3C, lanes 5–8). Figure 4B shows a representative single-molecule fluorescence trajectory of joining in the presence of dUTP^Q. After the

addition of extract, we observed a transition from a low FRET state to a high FRET state, indicating that short-range synopsis had occurred, followed by quenching in the high FRET state, which is consistent with dUTP^Q incorporation. Subsequent fluorescence fluctuations allowed us to unambiguously identify bona fide quenching events and exclude donor photobleaching. We ascribe the periodic return of donor fluorescence to quencher “blinking,” rather than repeated futile dUTP^Q incorporation attempts, as a minimal reconstitution showed fluorescence fluctuations following the initial quenching event, even after polymerase was removed (Figures S3D–S3L).

The vast majority (~80%) of quenching events occurred in the high FRET state (FRET_E ≈ 0.5; Figure 4C, blue), even though the

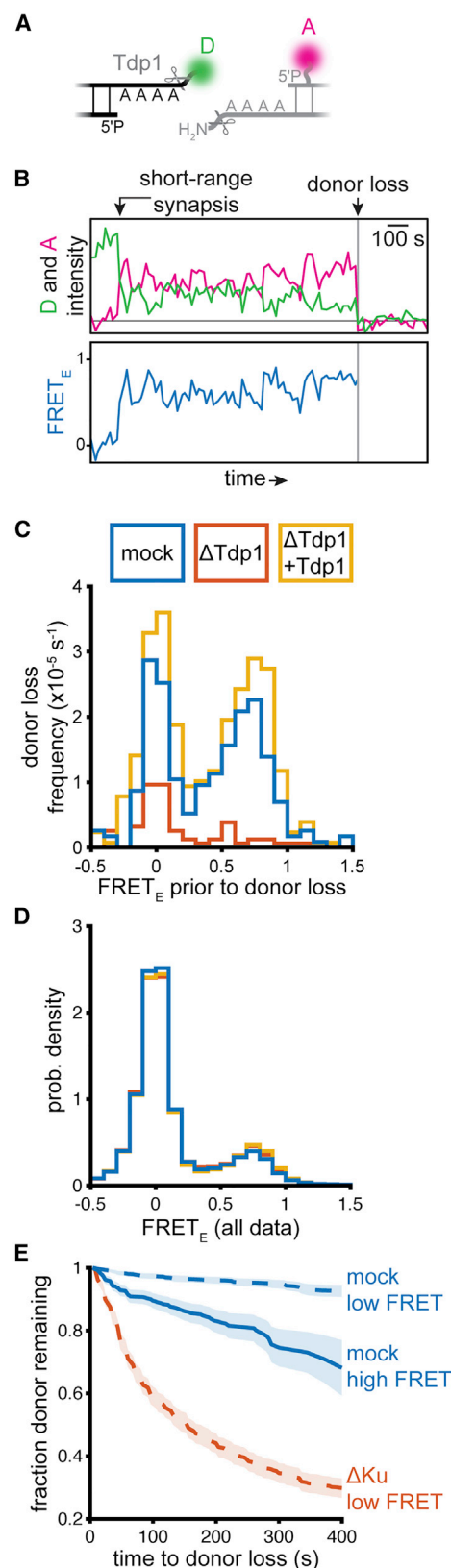


Figure 5. Short-Range Synthesis Accelerates Tdp1 Activity

(A) Experimental scheme for the single-molecule assay of Tdp1 activity and DNA-end synthesis. The DNA substrate was a derivative of the 3' adduct substrate depicted in Figure 2B (see Figure 1, 10 for chemical structure), with Cy3B conjugated to one of the 3' adducts. A, ATTO647N acceptor fluorophore; D, Cy3B donor fluorophore.

(B) Example trajectory. The Cy3B donor fluorophore was excited and donor emission (green) and ATTO647N acceptor emission (magenta) were recorded (top panel) and used to calculate FRET efficiency (blue, bottom panel). Scale bar, 100s.

(C) Frequency of donor loss events as a function of FRET efficiency immediately before donor loss under the indicated conditions. Blue, mock-depleted extracts (n = 222 events from 2 independent experiments); red, Tdp1-depleted extracts (n = 65 events from 2 independent experiments); yellow, Tdp1-depleted extracts supplemented with 40 nM recombinant Tdp1 (n = 339 events from 2 independent experiments). See Method Details for the calculation of the donor loss frequency and Figures S5D–S5F for the kinetic analysis and histograms represented as probability density.

(D) Histograms of FRET efficiency of all frames for all molecules before censoring. Colors as in (C).

(E) Donor survival kinetics (Kaplan-Meier estimate) under the indicated conditions. The x axis indicates dwell time in the high FRET (solid line) or low FRET (dashed lines) state before donor loss. Blue, donor survival kinetics in mock-depleted extract (n = 76 events, dashed line; 107 events, solid line); red, donor survival kinetics in Ku-depleted extract (n = 687 events); shaded areas, 95% confidence intervals.

low FRET state was much more abundant overall (FRET_E ≈ 0; Figure 4D, blue). Inclusion of deoxythymidine triphosphate (dTTP) instead of dUTP^Q revealed a background frequency of spuriously detected low FRET quenching events (Figure 4C, red), similar to that observed when dUTP^Q was present (Figure 4C, blue). Thus, dUTP^Q was efficiently incorporated in the high FRET state, and the rate of incorporation in the low FRET state was indistinguishable from the background rate (Figure 4E). Changing the template base from adenine to thymine, inclusion of dTTP instead of dUTP^Q, combined immunodepletion of pol λ and pol μ, or inhibition of DNA-PKcs suppressed dUTP^Q incorporation (Figure S3C, lanes 9–28) and high FRET quenching events (Figures 4C, yellow, S4B, and S4C). We conclude that pol λ activity is tightly coupled to the short-range synaptic complex.

Single-Molecule Imaging of Tdp1 Activity

We next asked whether Tdp1 also acts in the short-range synaptic complex. To measure Tdp1 activity on single DNA molecules, we conjugated the 3' adduct removed by Tdp1 (Figure 2B) to a donor fluorophore (Figure 5A). A DNA substrate with this modification on one end and an acceptor fluorophore in the duplex region of the other end allowed the observation of short-range synthesis via FRET and Tdp1 activity via loss of donor signal (Figure 5A). Ensemble experiments verified that the fluorescent 3' adduct was efficiently removed before joining (Figure S5A, lanes 1–4). To increase the efficiency of NHEJ-mediated synthesis in single-molecule experiments, we blocked the competing resection pathway by depleting extracts of the Mre11 nuclease, which did not significantly affect end processing or joining (Figure S5A, lanes 5–8). We frequently observed a transition from a low FRET state to a high FRET state followed by a loss of donor signal (e.g., Figure 5B). The majority (~60%) of donor loss events occurred

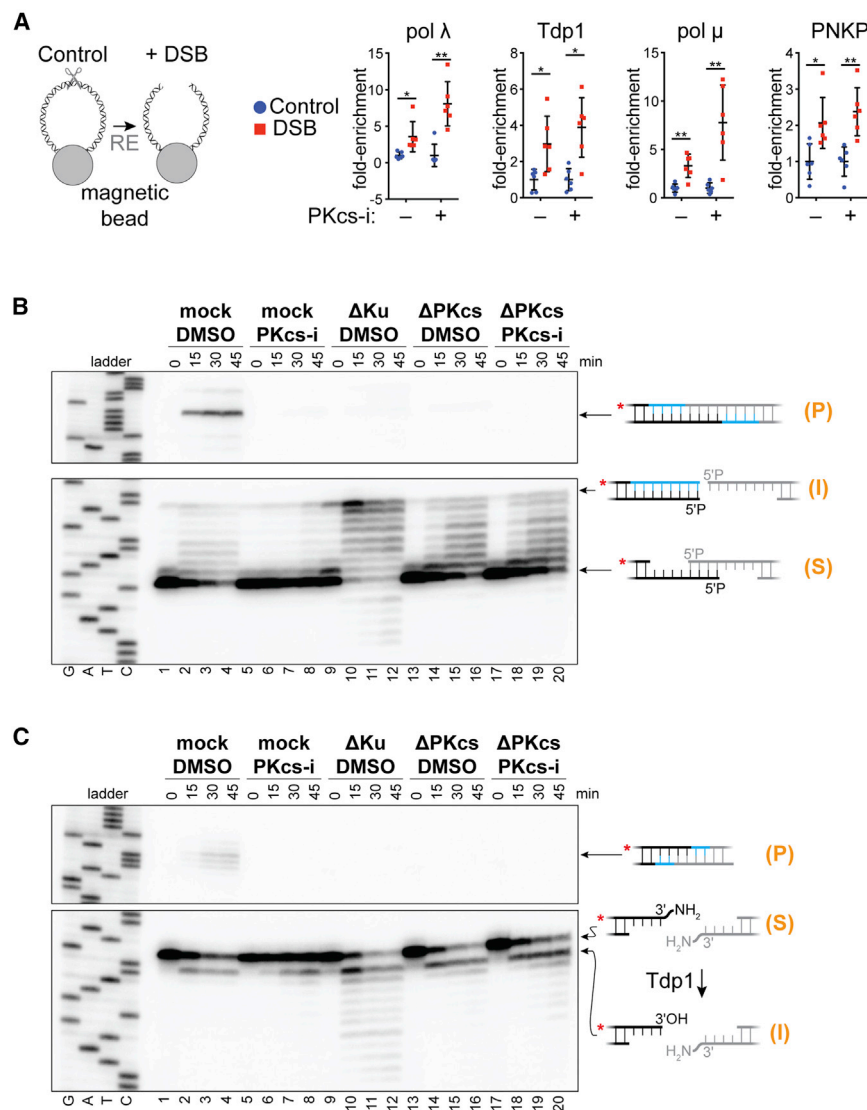


Figure 6. Ku Protects DNA Ends from Pre-mature and Off-Pathway Processing

(A) Western blot analysis of end-processing enzyme recruitment to a DSB (blunt ends introduced by XmnI digestion) in mock-treated or DNA-PKCs-inhibited extracts (see Figure S6A for a representative experiment and explanation of quantification). Fold enrichment is relative to undigested DNA ($n = 6$, mean \pm SD, * $p < 0.001$, ** $p < 0.001$, 2-tailed t test).

(B and C) Denaturing PAGE analysis of end processing and joining in the indicated extracts as in Figure 2. Panels differ by input DNA ends, depicted at right. I, processing intermediate; P, ligation product; S, input substrate.

Ku Protects Ends from Bound Processing Factors and Off-Pathway Enzymes

We next addressed how end processing is prevented before the formation of the short-range synaptic complex. One possibility is that short-range synapsis is required to recruit end-processing enzymes. To test this idea, we attached DNA to magnetic beads and isolated bound end-processing factors in the presence or absence of DNA-PKCs inhibitor, which blocks short-range synapsis (Figures 6A and S6A). However, as shown in Figure 6A, PNKP, pol λ , pol μ , and Tdp1 were each enriched on DSB-containing DNA relative to the intact control whether or not the short-range synaptic complex was allowed to form, suggesting that end-processing enzymes are recruited before short-range synapsis.

Based on the above results, we postulated that before short-range synapsis, core NHEJ factors protect DNA ends

from the bound processing factors. The immunodepletion of Ku (Figures S6B and S6C) caused aberrant fill-in of 5' overhang ends without subsequent joining (Figures 6B, lanes 9–12, and S6C, lanes 5–8), which is consistent with a role for Ku in DNA end protection (Liang and Jasin, 1996). The re-addition of recombinant Ku restored typical gap filling and joining (Figure S6C, lanes 9–12). Aberrant fill-in occurred even when pol λ and pol μ were immunodepleted in combination with Ku, suggesting that a non-NHEJ polymerase can fill in 5' overhangs when Ku is absent (Figure S6C, lanes 17–20). The addition of recombinant Ku to the Ku/pol λ /pol μ -depleted extract did not rescue gap filling and joining (Figure S6C, lanes 21–24), indicating that pol λ , which is required for NHEJ of these ends (Figure 2A), was functionally depleted in this experiment. Ku also suppressed aberrant 3' \rightarrow 5' exonuclease activity following 3' adduct removal (Figures 6C, lanes 9–12, and S6D, lanes 5–12). Combined immunodepletion of Ku and Tdp1 (Figure S6D) prevented both 3' adduct removal and exonuclease activity (Figure S6D, lanes 17–20),

in the high FRET state (Figure 5C, blue), despite its overall low abundance ($\sim 20\%$ of all frames; Figure 5D, blue). Thus, donor loss occurred ~ 5 -fold more quickly in the high FRET state compared to the low FRET state (Figure 5E, solid blue versus dashed blue). Tdp1 immunodepletion greatly reduced the frequency of donor loss events from both low and high FRET states (Figure 5C, red), and this reduction was rescued upon the re-addition of recombinant Tdp1 (Figure 5C, yellow), indicating that Tdp1 and not photobleaching was responsible for the vast majority of the detected donor loss events. The occasional donor loss events observed in the low FRET state likely involve Tdp1 acting on transiently unprotected ends (see below). In summary, all of the processing reactions measured depended on the formation of the short-range complex (Figures 3 and S2), and in at least two of these—gap filling and adduct removal—end processing occurred preferentially in the high FRET state (Figures 4 and 5). The data suggest that processing generally occurs within the short-range complex.

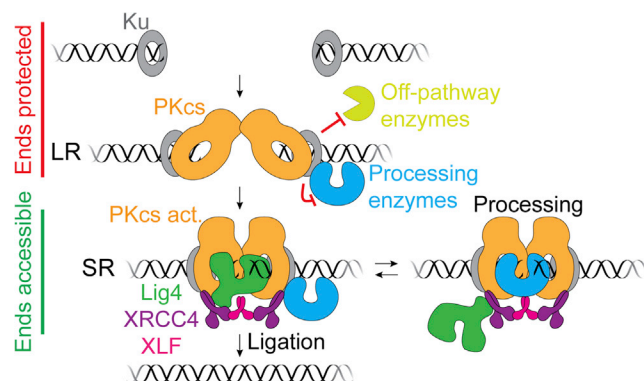


Figure 7. Model of DNA End Processing during NHEJ

and the re-addition of recombinant Tdp1 restored these activities (Figure S6D, lanes 21–24). Thus, Tdp1 can access DNA ends in the absence of Ku, but ends are protected in the presence of Ku when short-range synapsis is blocked (Figures 3B and 6C, lanes 5–9). In addition, Ku depletion resulted in aberrant nuclease activity on blunt ends, 3' overhang ends lacking microhomology, and 5' overhang ends with internal microhomology (Figures S6E–S6G). Thus, Ku protects DNA ends from processing by both NHEJ and off-pathway enzymes.

DNA-PKcs has also been reported to protect ends from processing (Chan and Lees-Miller, 1996; Cui et al., 2005; Ding et al., 2003; Dobbs et al., 2010; Goodarzi et al., 2006; Reddy et al., 2004). Consistent with this idea, whereas the inhibition of DNA-PKcs suppressed end processing (Figures 6B, lanes 5–8, and 6C, lanes 5–8), the immunodepletion of DNA-PKcs resulted in the aberrant processing of 5' overhangs and 3' adducted ends, although to a lesser extent than the immunodepletion of Ku (Figures 6B, lanes 9–16, and 6C, lanes 9–16). The inhibition of DNA-PKcs had no effect on DNA-PKcs-depleted extracts (Figures 6B, lanes 17–20, and 6C, lanes 17–20), indicating that DNA-PKcs was functionally depleted in these experiments. The addition of human DNA-PKcs to DNA-PKcs-depleted extracts did not restore end joining (data not shown), either because DNA-PKcs depletion co-depleted a critical unknown factor or due to an inability of the human protein to cooperate with *Xenopus* NHEJ factors. We conclude that before short-range synapsis, Ku and DNA-PKcs protect DNA ends from premature processing, with Ku playing the major protective role. Subsequently, ends become accessible for processing upon short-range synapsis.

As shown above, Tdp1 had measurable activity outside the short-range synaptic complex (Figures 5C and S5B). We postulated that Tdp1 acts on DNA ends if they are transiently unprotected before short-range synapsis. Consistent with this idea and the above ensemble experiments (Figure 6C), Ku immunodepletion in the single-molecule Tdp1 assay (Figure 5A) resulted in rapid donor loss from the low-FRET state (Figures 5E, red dashed line, and S5C, red), and this effect was suppressed by the re-addition of recombinant Ku (Figure S5C, yellow). Tdp1 has known roles outside NHEJ and does not typically alter the DNA sequence (El-Khamisy and Caldecott, 2006). These traits

may explain the less stringent coupling of Tdp1 activity to the formation of the short-range synaptic complex.

DISCUSSION

Our findings reveal how NHEJ minimizes mutagenesis without sacrificing the versatility needed to repair diverse DSBs (Figure 7). Both before ends undergo synapsis and within the long-range synaptic complex, Ku and DNA-PKcs protect DNA ends from unrestricted processing. Thereafter, formation of the short-range synaptic complex potentiates the action of the DNA end processing machinery. Within the short-range synaptic complex, processing of a given end is dictated by the structure of its synapsed partner. For example, a 3' overhang was directly ligated to a complementary 3' overhang (Figure 1, 3) or blunt end (Figure 1, 8), but was extended by pol μ when synapsed with a non-complementary 3' overhang (Figure 1, 8). Thus, end processing depends on short-range synapsis and is tailored to the synapsed ends. These features minimize mutagenesis in multiple ways. First, because Lig4 is required for short-range synapsis, compatible DNA ends have a high probability of undergoing ligation without processing, as seen in extracts (Figure 1, 1–3) and cells (Waters et al., 2014b). Second, as soon as incompatible ends become compatible, they undergo ligation, thus avoiding unnecessary processing. For example, in Figure 1B, 9, nuclease activity is limited to flap removal. Third, short-range synapsis promotes the use of pre-existing microhomology (Figure 1B, 4, 5, and 9). This feature helps preserve the original sequence in cases in which DSBs retain base complementarity but have damaged, unligatable termini, such as 3'-phosphoglycolates introduced by ionizing radiation (Povirk, 2012). Finally, the maintenance of short-range synapsis during processing avoids unpaired-end intermediates that may give rise to translocations. Notably, Lig4-XRCC4, XLF, and/or DNA-PKcs activities have been implicated in NHEJ polymerase or nuclease activity in human cell extracts (Akopiants et al., 2009; Budman et al., 2007; Lee et al., 2003, 2004) and human cells (Celli and de Lange, 2005; Ding et al., 2003), which is consistent with our model of end processing regulation.

Lig4-XRCC4 Dynamics during Joining of Incompatible Ends

To explain how ligation is prioritized over end processing during NHEJ, we propose that Lig4 directly engages DNA ends to drive short-range synapsis (Figure 7). Such DNA bridging may constitute the non-catalytic role of Lig4 in synapsis that we and others have observed (Cottarel et al., 2013; Graham et al., 2016). Whereas Ku and DNA-PKcs protect ends before short-range synapsis (Figure 6), we speculate that Lig4 itself acts as an end protection factor in the short-range synaptic complex by excluding processing enzymes before ligation has been attempted. To facilitate the processing of incompatible ends, we propose that Lig4 dynamically releases DNA ends to allow processing and promptly re-engages them to ensure the ligation of minimally processed ends (Figure 7). We recently reported that a single XLF dimer interacts with two XRCC4-Lig4 complexes to mediate short-range synapsis (Figure 7; Graham et al.,

2018). Thus, after initial DNA end binding by Lig4, an XRCC4-XLF-XRCC4 “bridge” may maintain short-range synapsis, allowing Lig4 to release DNA ends for processing while remaining in the synaptic complex via its XRCC4 interaction. Alternatively, short-range synapsis may be established and maintained by another non-catalytic function of Lig4, such as XRCC4 recruitment. End protection by Ku and DNA-PKcs must also be relieved to allow processing and ligation. This deprotection may occur through Ku translocation away from the break (Yoo and Dynan, 1999) and/or autophosphorylation-induced conformational changes or dissociation of DNA-PKcs (Chan and Lees-Miller, 1996; Cui et al., 2005; Ding et al., 2003; Dobbs et al., 2010; Goodarzi et al., 2006; Reddy et al., 2004). Whereas Lig4 promotes local processing by NHEJ enzymes, long-range DSB resection by BLM/EXO1/DNA2 does not require Lig4 (Canela et al., 2016; Dorsett et al., 2014), which is indicative of distinct regulation (Setiawati and Durocher, 2019; Symington, 2014). In summary, our results imply that mutagenesis during NHEJ is minimized by carefully restricting the access of processing factors to DNA ends, both before and after the ends have undergone synapsis.

Hierarchical Access of End-Modifying Enzymes

Our results provide two lines of evidence that NHEJ minimizes errors not only by prioritizing ligation but also by using processing enzymes hierarchically, as recently proposed (Strande et al., 2012; Waters et al., 2014a). First, we find that conservative end processing events are favored over sequence-altering events. For example, ends requiring only 5′ phosphorylation for ligation are almost always joined without insertions or deletions (Figure 2C, lanes 1–4). Moreover, when PNKP is absent, such ends are not subject to significant polymerase or nuclease activity (Figure 2C, lanes 5–8). Thus, PNKP sits atop the processing hierarchy for these ends. Similarly, Tdp1 activity is preferred to nuclease activity in the removal of 3′ adducts (Figure 2B). Second, although non-complementary ends could be rendered ligatable through polymerase or nuclease activity, we observed a strong preference for the former (Figure 1B, 4–9). These features may contribute to repair fidelity as follows (Figure S7A): Lig4, PNKP, and Tdp1 repair ends without altering sequence and are positioned at the top of the utilization hierarchy. In the next tier, pol λ and pol μ alter sequence, but they are limited in the extent of modification by the availability of the single-stranded template (pol μ has reported template-independent synthesis activity, but it is much less efficient than templated synthesis; Nick McElhinny et al., 2005). Finally, nucleases could theoretically resolve any form of damage found at a DNA end, but they are used as a last resort, owing to their mutagenicity. Future experiments will be necessary to determine the mechanism underlying this hierarchy. Together, confinement of end processing to the short-range synaptic complex and hierarchical utilization of processing enzymes finely tune the processing of DNA ends to minimize errors during DSB repair via NHEJ.

Regulation of End Processing in V(D)J Recombination

V(D)J recombination assembles immunoglobulin and T cell receptor genes by introducing programmed DSBs that are repaired by NHEJ (Figure S7B; Alt et al., 2013; Gellert, 2002).

“Coding ends” generated by the recombination-activating gene (RAG) recombinase are joined to form the exon encoding the antigen-binding region. Coding ends exhibit substantial variation in the number of nucleotides inserted or deleted before joining (Figure S7C), thereby augmenting immune receptor diversity. How NHEJ promotes the highly mutagenic processing of coding ends but not of spontaneous DSBs is an important question. Because the same core NHEJ factors direct both processes, we hypothesize that the overarching regulation of end processing is similar, but that V(D)J recombination includes at least two unique features that promote junctional variability. For example, RAG generates a hairpin terminus at coding ends, which the Artemis nuclease must cut before ligation can be attempted. First, whereas ligation is usually attempted before end processing for spontaneous DSBs, coding ends always require initial processing. Importantly, Artemis preferentially cleaves the hairpin two-nucleotide 3′ of the hairpin tip, generating four-nucleotide 3′ overhangs that are usually non-complementary (Ma et al., 2002; Schissel, 1998). Of the ends tested in this study, such a substrate had the most variable junctions (Figure 1B, 6), although this variability was still largely limited to one- to four-nucleotide insertions mediated by pol μ . Second, V(D)J recombination uses the lymphocyte-specific terminal deoxynucleotidyl transferase (TdT), which has robust template-independent synthesis activity on 3′ overhangs (Deng and Wu, 1983). Signal ends (Figure S7C), which are blunt and therefore do not require Artemis activity and do not present the preferred TdT substrate, are typically joined without any insertions or deletions (Gellert, 2002), similar to compatible spontaneous DSBs (Figure 1B, 1–3). An alternative view is that the processing of coding ends and spontaneous DSB breaks is regulated by entirely distinct mechanisms. For example, based on reconstitution with purified NHEJ factors, coding ends may independently and stochastically recruit processing factors until ends become compatible for ligation (Lieber, 2010; Ma et al., 2004). Ultimately, to resolve how end processing is regulated during V(D)J recombination, it will be critical to understand how RAG transfers coding ends to the NHEJ machinery (Bertocci et al., 2003, 2006; Lee et al., 2004b; Ma et al., 2004; Mahajan et al., 2002).

Gene Editing

Because NHEJ is the predominant pathway for the repair of CRISPR-Cas9 DSBs, our results have important implications for genome engineering. Efforts to improve the efficiency of CRISPR-Cas9-mediated gene disruption by overexpressing DSB processing enzymes have been only modestly effective (Chari et al., 2015), most likely because such an approach does not circumvent DNA end protection before short-range synapsis or immediate ligation of compatible ends upon short-range synapsis. Our model predicts that a more effective approach will be to increase DNA end accessibility before ligation, thereby facilitating the activity of processing enzymes.

Conclusion

In summary, we find that the integration of DNA processing with the formation of higher-order DNA repair complexes helps to

ensure the fidelity of NHEJ. A similar strategy may govern other crucial events in DNA repair, such as 5'→3' resection of DSBs, which initiates homologous recombination (HR) and alternative end joining (Symington and Gautier, 2011). For example, tethering two broken DNA ends to each other could trigger their simultaneous resection (Andres et al., 2015; Westmoreland and Resnick, 2013). In addition, resection may depend on tethering a broken end to its intact sister chromatid (Williams et al., 2008; Zhu et al., 2018), preventing excessive resection when a homology donor is not available. For these and other questions in the regulation of DNA metabolism, approaches that correlate the structural features of protein-DNA complexes with DNA modification will serve as powerful tools.

STAR★METHODS

Detailed methods are provided in the online version of this paper and include the following:

- KEY RESOURCES TABLE
- LEAD CONTACT AND MATERIALS AVAILABILITY
- EXPERIMENTAL MODEL AND SUBJECT DETAILS
- METHOD DETAILS
 - Egg extract preparation
 - Preparation of DNA substrates
 - Preparation of fluorescently-labeled oligonucleotides
 - Preparation of dUTP^Q
 - Protein expression and purification
 - Antibodies and immunodepletion
 - Immunoblotting
 - Ensemble NHEJ assays
 - Deep sequencing of NHEJ products
 - Single-molecule microscope and chamber preparation
 - Analysis of single-molecule data
 - Single-molecule assay for polymerase activity
 - Single-molecule assay for Tdp1 activity
 - DNA-pulldown and analysis of protein enrichment on DSBs
- QUANTIFICATION AND STATISTICAL ANALYSIS
- DATA AND CODE AVAILABILITY

SUPPLEMENTAL INFORMATION

Supplemental Information can be found online at <https://doi.org/10.1016/j.molcel.2019.11.018>.

ACKNOWLEDGMENTS

We thank R. Scully, T. Graham, I. Rivera, V. Kumar, and members of the Walter and Loparo laboratories for helpful discussions and comments on the manuscript. This work was supported by NIH grant R01GM115487 (to J.J.L.) and the Howard Hughes Medical Institute (to J.C.W.). B.M.S. is supported by a postdoctoral fellowship from the Damon Runyon Cancer Research Foundation. A.T.M. is supported by a postdoctoral fellowship from the American Cancer Society. J.C.W. is an investigator of the Howard Hughes Medical Institute.

AUTHOR CONTRIBUTIONS

B.M.S. performed all of the experiments, with the exception of the DNA pull-down experiments, which were performed by A.T.M. J.J.L., J.C.W., and

B.M.S. conceived the experiments, analyzed the data, and wrote the paper, with input from A.T.M.

DECLARATION OF INTERESTS

The authors declare no competing interests.

Received: July 16, 2019
Revised: October 9, 2019
Accepted: November 22, 2019
Published: December 17, 2019

REFERENCES

- Ahel, I., Rass, U., El-Khamisy, S.F., Katyal, S., Clements, P.M., McKinnon, P.J., Caldecott, K.W., and West, S.C. (2006). The neurodegenerative disease protein aprataxin resolves abortive DNA ligation intermediates. *Nature* 443, 713–716.
- Ahnesorg, P., Smith, P., and Jackson, S.P. (2006). XLF interacts with the XRCC4-DNA ligase IV complex to promote DNA nonhomologous end-joining. *Cell* 124, 301–313.
- Akopiants, K., Zhou, R.Z., Mohapatra, S., Valerie, K., Lees-Miller, S.P., Lee, K.J., Chen, D.J., Revy, P., de Villartay, J.P., and Povirk, L.F. (2009). Requirement for XLF/Cernunnos in alignment-based gap filling by DNA polymerases λ and μ for nonhomologous end joining in human whole-cell extracts. *Nucleic Acids Res.* 37, 4055–4062.
- Alt, F.W., Zhang, Y., Meng, F.L., Guo, C., and Schwer, B. (2013). Mechanisms of programmed DNA lesions and genomic instability in the immune system. *Cell* 152, 417–429.
- Andres, S.N., Appel, D.C., Westmoreland, J.W., Williams, J.S., Nguyen, Y., Robertson, P.D., Resnick, M.A., and Williams, S.R. (2015). Tetrameric Ctp1 coordinates DNA binding and DNA bridging in DNA double-strand-break repair. *Nat. Struct. Mol. Biol.* 22, 158–166.
- Aparicio, T., Baer, R., and Gautier, J. (2014). DNA double-strand break repair pathway choice and cancer. *DNA Repair (Amst.)* 19, 169–175.
- Baumann, P., and West, S. (1998). DNA end-joining catalyzed by human cell-free extracts. *Proc National Acad Sci* 95, 14066–14070.
- Bertocci, B., De Smet, A., Berek, C., Weill, J.C., and Reynaud, C.A. (2003). Immunoglobulin κ light chain gene rearrangement is impaired in mice deficient for DNA polymerase μ . *Immunity* 19, 203–211.
- Bertocci, B., De Smet, A., Weill, J.C., and Reynaud, C.A. (2006). Nonoverlapping functions of DNA polymerases μ , λ , and terminal deoxynucleotidyltransferase during immunoglobulin V(D)J recombination in vivo. *Immunity* 25, 31–41.
- B  termier, M., Bertrand, P., and Lopez, B.S. (2014). Is non-homologous end-joining really an inherently error-prone process? *PLoS Genet.* 10, e1004086.
- Budman, J., and Chu, G. (2005). Processing of DNA for nonhomologous end-joining by cell-free extract. *EMBO J.* 24, 849–860.
- Budman, J., Kim, S.A., and Chu, G. (2007). Processing of DNA for nonhomologous end-joining is controlled by kinase activity and XRCC4/ligase IV. *J. Biol. Chem.* 282, 11950–11959.
- Canela, A., Sridharan, S., Sciascia, N., Tubbs, A., Meltzer, P., Sleckman, B.P., and Nussenzweig, A. (2016). DNA Breaks and End Resection Measured Genome-wide by End Sequencing. *Mol. Cell* 63, 898–911.
- Celli, G.B., and de Lange, T. (2005). DNA processing is not required for ATM-mediated telomere damage response after TRF2 deletion. *Nat. Cell Biol.* 7, 712–718.
- Chan, D.W., and Lees-Miller, S.P. (1996). The DNA-dependent protein kinase is inactivated by autophosphorylation of the catalytic subunit. *J. Biol. Chem.* 271, 8936–8941.
- Chang, H.H., Watanabe, G., and Lieber, M.R. (2015). Unifying the DNA end-processing roles of the artemis nuclease: Ku-dependent artemis resection at blunt DNA ends. *J. Biol. Chem.* 290, 24036–24050.

- Chari, R., Mali, P., Moosburner, M., and Church, G.M. (2015). Unraveling CRISPR-Cas9 genome engineering parameters via a library-on-library approach. *Nat. Methods* 12, 823–826.
- Chiruvella, K.K., Liang, Z., and Wilson, T.E. (2013). Repair of double-strand breaks by end joining. *Cold Spring Harb. Perspect. Biol.* 5, a012757.
- Clements, P.M., Breslin, C., Deeks, E.D., Byrd, P.J., Ju, L., Bieganski, P., Brenner, C., Moreira, M.C., Taylor, A.M., and Caldecott, K.W. (2004). The ataxia-oculomotor apraxia 1 gene product has a role distinct from ATM and interacts with the DNA strand break repair proteins XRCC1 and XRCC4. *DNA Repair (Amst.)* 3, 1493–1502.
- Conlin, M.P., Reid, D.A., Small, G.W., Chang, H.H., Watanabe, G., Lieber, M.R., Ramsden, D.A., and Rothenberg, E. (2017). DNA Ligase IV Guides End-Processing Choice during Nonhomologous End Joining. *Cell Rep.* 20, 2810–2819.
- Cortes Ledesma, F., El Khamisy, S.F., Zuma, M.C., Osborn, K., and Caldecott, K.W. (2009). A human 5'-tyrosyl DNA phosphodiesterase that repairs topoisomerase-mediated DNA damage. *Nature* 461, 674–678.
- Cottarel, J., Frit, P., Bombarde, O., Salles, B., Négrel, A., Bernard, S., Jeggo, P.A., Lieber, M.R., Modesti, M., and Calsou, P. (2013). A noncatalytic function of the ligation complex during nonhomologous end joining. *J. Cell Biol.* 200, 173–186.
- Cui, X., Yu, Y., Gupta, S., Cho, Y.M., Lees-Miller, S.P., and Meek, K. (2005). Autophosphorylation of DNA-dependent protein kinase regulates DNA end processing and may also alter double-strand break repair pathway choice. *Mol. Cell Biol.* 25, 10842–10852.
- Davis, A.J., Chen, B.P., and Chen, D.J. (2014). DNA-PK: a dynamic enzyme in a versatile DSB repair pathway. *DNA Repair (Amst.)* 17, 21–29.
- Deng, G., and Wu, R. (1983). Terminal transferase: use of the tailing of DNA and for in vitro mutagenesis. *Methods Enzymol.* 100, 96–116.
- Di Virgilio, M., and Gautier, J. (2005). Repair of double-strand breaks by nonhomologous end joining in the absence of Mre11. *J. Cell Biol.* 171, 765–771.
- Ding, Q., Reddy, Y.V., Wang, W., Woods, T., Douglas, P., Ramsden, D.A., Lees-Miller, S.P., and Meek, K. (2003). Autophosphorylation of the catalytic subunit of the DNA-dependent protein kinase is required for efficient end processing during DNA double-strand break repair. *Mol. Cell Biol.* 23, 5836–5848.
- Dobbs, T.A., Tainer, J.A., and Lees-Miller, S.P. (2010). A structural model for regulation of NHEJ by DNA-PKcs autophosphorylation. *DNA Repair (Amst.)* 9, 1307–1314.
- Dorsett, Y., Zhou, Y., Tubbs, A.T., Chen, B.R., Purman, C., Lee, B.S., George, R., Bredemeyer, A.L., Zhao, J.Y., Sodergren, E., et al. (2014). HCoDES reveals chromosomal DNA end structures with single-nucleotide resolution. *Mol. Cell* 56, 808–818.
- El-Khamisy, S.F., and Caldecott, K.W. (2006). TDP1-dependent DNA single-strand break repair and neurodegeneration. *Mutagenesis* 21, 219–224.
- Falck, J., Coates, J., and Jackson, S.P. (2005). Conserved modes of recruitment of ATM, ATR and DNA-PKcs to sites of DNA damage. *Nature* 434, 605–611.
- Feldmann, E., Schmiemann, V., Goedecke, W., Reichenberger, S., and Pfeiffer, P. (2000). DNA double-strand break repair in cell-free extracts from Ku80-deficient cells: implications for Ku serving as an alignment factor in non-homologous DNA end joining. *Nucleic Acids Res* 28, 2585–2596.
- Gellert, M. (2002). V(D)J recombination: RAG proteins, repair factors, and regulation. *Annu. Rev. Biochem.* 71, 101–132.
- Gómez-Herreros, F., Romero-Granados, R., Zeng, Z., Alvarez-Quilón, A., Quintero, C., Ju, L., Umans, L., Vermeire, L., Huylebroeck, D., Caldecott, K.W., and Cortés-Ledesma, F. (2013). TDP2-dependent non-homologous end-joining protects against topoisomerase II-induced DNA breaks and genome instability in cells and in vivo. *PLoS Genet.* 9, e1003226.
- Goodarzi, A.A., Yu, Y., Riballo, E., Douglas, P., Walker, S.A., Ye, R., Härer, C., Marchetti, C., Morrice, N., Jeggo, P.A., and Lees-Miller, S.P. (2006). DNA-PK autophosphorylation facilitates Artemis endonuclease activity. *EMBO J.* 25, 3880–3889.
- Gottlieb, T.M., and Jackson, S.P. (1993). The DNA-dependent protein kinase: requirement for DNA ends and association with Ku antigen. *Cell* 72, 131–142.
- Graham, T.G., Walter, J.C., and Loparo, J.J. (2016). Two-Stage Synapsis of DNA Ends during Non-homologous End Joining. *Mol. Cell* 61, 850–858.
- Graham, T., Walter, J.C., and Loparo, J.J. (2017). Ensemble and Single-Molecule Analysis of Non-Homologous End Joining in Frog Egg Extracts. *Methods Enzymol.* 591, 233–270.
- Graham, T.G.W., Carney, S.M., Walter, J.C., and Loparo, J.J. (2018). A single XLF dimer bridges DNA ends during nonhomologous end joining. *Nat. Struct. Mol. Biol.* 25, 877–884.
- Grawunder, U., Wilm, M., Wu, X., Kulesza, P., Wilson, T.E., Mann, M., and Lieber, M.R. (1997). Activity of DNA ligase IV stimulated by complex formation with XRCC4 protein in mammalian cells. *Nature* 388, 492–495.
- Guirouilh-Barbat, J., Huck, S., Bertrand, P., Pirzio, L., Desmazière, C., Sabatier, L., and Lopez, B.S. (2004). Impact of the KU80 pathway on NHEJ-induced genome rearrangements in mammalian cells. *Mol. Cell* 14, 611–623.
- Inamdar, K.V., Pouliot, J.J., Zhou, T., Lees-Miller, S.P., Rasouli-Nia, A., and Povirk, L.F. (2002). Conversion of phosphoglycolate to phosphate termini on 3' overhangs of DNA double strand breaks by the human tyrosyl-DNA phosphodiesterase hTdp1. *J. Biol. Chem.* 277, 27162–27168.
- Interthal, H., Chen, H.J., and Champoux, J.J. (2005). Human Tdp1 cleaves a broad spectrum of substrates, including phosphoamide linkages. *J. Biol. Chem.* 280, 36518–36528.
- Jette, N., and Lees-Miller, S.P. (2015). The DNA-dependent protein kinase: a multifunctional protein kinase with roles in DNA double strand break repair and mitosis. *Prog. Biophys. Mol. Biol.* 117, 194–205.
- Karanam, K., Kafri, R., Loewer, A., and Lahav, G. (2012). Quantitative live cell imaging reveals a gradual shift between DNA repair mechanisms and a maximal use of HR in mid S phase. *Mol. Cell* 47, 320–329.
- Koch, C.A., Agyei, R., Galicia, S., Metalnikov, P., O'Donnell, P., Starostine, A., Weinfeld, M., and Durocher, D. (2004). Xrcc4 physically links DNA end processing by polynucleotide kinase to DNA ligation by DNA ligase IV. *EMBO J.* 23, 3874–3885.
- Kumar, V., Alt, F.W., and Frock, R.L. (2016). PAXX and XLF DNA repair factors are functionally redundant in joining DNA breaks in a G1-arrested progenitor B-cell line. *Proc. Natl. Acad. Sci. USA* 113, 10619–10624.
- Labhart, P. (1999). Ku-dependent nonhomologous DNA end joining in *Xenopus* egg extracts. *Mol. Cell Biol.* 19, 2585–2593.
- Lebofsky, R., Takahashi, T., and Walter, J.C. (2009). DNA replication in nucleus-free *Xenopus* egg extracts. *Methods Mol. Biol.* 521, 229–252.
- Lee, J.W., Yannone, S.M., Chen, D.J., and Povirk, L.F. (2003). Requirement for XRCC4 and DNA ligase IV in alignment-based gap filling for nonhomologous DNA end joining in vitro. *Cancer Res.* 63, 22–24.
- Lee, J.W., Blanco, L., Zhou, T., Garcia-Diaz, M., Bebenek, K., Kunkel, T.A., Wang, Z., and Povirk, L.F. (2004b). Implication of DNA polymerase λ in alignment-based gap filling for nonhomologous DNA end joining in human nuclear extracts. *J. Biol. Chem.* 279, 805–811.
- Lees-Miller, S.P., Chen, Y.R., and Anderson, C.W. (1990). Human cells contain a DNA-activated protein kinase that phosphorylates simian virus 40 T antigen, mouse p53, and the human Ku autoantigen. *Mol. Cell Biol.* 10, 6472–6481.
- Liang, F., and Jasin, M. (1996). Ku80-deficient cells exhibit excess degradation of extrachromosomal DNA. *J. Biol. Chem.* 271, 14405–14411.
- Lieber, M.R. (2010). The mechanism of double-strand DNA break repair by the nonhomologous DNA end-joining pathway. *Annu. Rev. Biochem.* 79, 181–211.
- Lin, Y., Lukacsovich, T., and Waldman, A.S. (1999). Multiple pathways for repair of DNA double-strand breaks in mammalian chromosomes. *Mol. Cell Biol.* 19, 8353–8360.
- Lin, W.Y., Wilson, J.H., and Lin, Y. (2013). Repair of chromosomal double-strand breaks by precise ligation in human cells. *DNA Repair (Amst.)* 12, 480–487.

- Lukacsovich, T., Yang, D., and Waldman, A.S. (1994). Repair of a specific double-strand break generated within a mammalian chromosome by yeast endonuclease I-SceI. *Nucleic Acids Res.* 22, 5649–5657.
- Ma, Y., Pannicke, U., Schwarz, K., and Lieber, M.R. (2002). Hairpin opening and overhang processing by an Artemis/DNA-dependent protein kinase complex in nonhomologous end joining and V(D)J recombination. *Cell* 108, 781–794.
- Ma, Y., Lu, H., Tiffin, B., Goodman, M.F., Shimazaki, N., Koiwai, O., Hsieh, C.L., Schwarz, K., and Lieber, M.R. (2004). A biochemically defined system for mammalian nonhomologous DNA end joining. *Mol. Cell* 16, 701–713.
- Mahajan, K.N., Nick McElhinny, S.A., Mitchell, B.S., and Ramsden, D.A. (2002). Association of DNA polymerase μ (pol μ) with Ku and ligase IV: role for pol μ in end-joining double-strand break repair. *Mol. Cell. Biol.* 22, 5194–5202.
- Mimori, T., Hardin, J.A., and Steitz, J.A. (1986). Characterization of the DNA-binding protein antigen Ku recognized by autoantibodies from patients with rheumatic disorders. *J. Biol. Chem.* 261, 2274–2278.
- Nick McElhinny, S.A., Havener, J.M., Garcia-Diaz, M., Juárez, R., Bebenek, K., Kee, B.L., Blanco, L., Kunkel, T.A., and Ramsden, D.A. (2005). A gradient of template dependence defines distinct biological roles for family X polymerases in nonhomologous end joining. *Mol. Cell* 19, 357–366.
- Ochi, T., Blackford, A.N., Coates, J., Jhuji, S., Mehmood, S., Tamura, N., Travers, J., Wu, Q., Draviam, V.M., Robinson, C.V., et al. (2015). DNA repair. PAXX, a paralog of XRCC4 and XLF, interacts with Ku to promote DNA double-strand break repair. *Science* 347, 185–188.
- Pfeiffer, P., and Vielmetter, W. (1988). Joining of nonhomologous DNA double strand breaks in vitro. *Nucleic Acids Res.* 16, 907–924.
- Phillips, J.W., and Morgan, W.F. (1994). Illegitimate recombination induced by DNA double-strand breaks in a mammalian chromosome. *Mol. Cell. Biol.* 14, 5794–5803.
- Povirk, L.F. (2012). Processing of damaged DNA ends for double-strand break repair in mammalian cells. *ISRN Mol. Biol.* 2012, 1–16.
- Preus, S., Noer, S.L., Hildebrandt, L.L., Gudnason, D., and Birkedal, V. (2015). iSMS: single-molecule FRET microscopy software. *Nat. Methods* 12, 593–594.
- Radhakrishnan, S.K., Jette, N., and Lees-Miller, S.P. (2014). Non-homologous end joining: emerging themes and unanswered questions. *DNA Repair (Amst.)* 17, 2–8.
- Reddy, Y.V., Ding, Q., Lees-Miller, S.P., Meek, K., and Ramsden, D.A. (2004). Non-homologous end joining requires that the DNA-PK complex undergo an autophosphorylation-dependent rearrangement at DNA ends. *J. Biol. Chem.* 279, 39408–39413.
- Reid, D.A., Conlin, M.P., Yin, Y., Chang, H.H., Watanabe, G., Lieber, M.R., Ramsden, D.A., and Rothenberg, E. (2017). Bridging of double-stranded breaks by the nonhomologous end-joining ligation complex is modulated by DNA end chemistry. *Nucleic Acids Res.* 45, 1872–1878.
- Rouet, P., Smith, F., and Jasin, M. (1994). Introduction of double-strand breaks into the genome of mouse cells by expression of a rare-cutting endonuclease. *Mol. Cell. Biol.* 14, 8096–8106.
- Sargent, R.G., Breneman, M.A., and Wilson, J.H. (1997). Repair of site-specific double-strand breaks in a mammalian chromosome by homologous and illegitimate recombination. *Mol. Cell. Biol.* 17, 267–277.
- Schlissel, M.S. (1998). Structure of nonhairpin coding-end DNA breaks in cells undergoing V(D)J recombination. *Mol. Cell. Biol.* 18, 2029–2037.
- Setiawati, D., and Durocher, D. (2019). Shieldin - the protector of DNA ends. *EMBO Rep.* 20, e47560.
- Sibanda, B.L., Chirgadze, D.Y., Ascher, D.B., and Blundell, T.L. (2017). DNA-PKcs structure suggests an allosteric mechanism modulating DNA double-strand break repair. *Science* 355, 520–524.
- Strande, N.T., Waters, C.A., and Ramsden, D.A. (2012). Resolution of complex ends by Nonhomologous end joining - better to be lucky than good? *Genome Integr.* 3, 10.
- Symington, L.S. (2014). End resection at double-strand breaks: mechanism and regulation. *Cold Spring Harb. Perspect. Biol.* 6, a016436.
- Symington, L.S., and Gautier, J. (2011). Double-strand break end resection and repair pathway choice. *Annu. Rev. Genet.* 45, 247–271.
- Tadi, S.K., Tellier-Lebègue, C., Nemoz, C., Drevet, P., Audebert, S., Roy, S., Meek, K., Charbonnier, J.B., and Modesti, M. (2016). PAXX Is an Accessory c-NHEJ Factor that Associates with Ku70 and Has Overlapping Functions with XLF. *Cell Rep.* 17, 541–555.
- Thode, S., Schäfer, A., Pfeiffer, P., and Vielmetter, W. (1990). A novel pathway of DNA end-to-end joining. *Cell* 60, 921–928.
- van de Meent, J.W., Bronson, J.E., Wiggins, C.H., and Gonzalez, R.L., Jr. (2014). Empirical Bayes methods enable advanced population-level analyses of single-molecule FRET experiments. *Biophys. J.* 106, 1327–1337.
- Walker, J.R., Corpina, R.A., and Goldberg, J. (2001). Structure of the Ku heterodimer bound to DNA and its implications for double-strand break repair. *Nature* 412, 607–614.
- Walter, J., and Newport, J.W. (1997). Regulation of replicon size in *Xenopus* egg extracts. *Science* 275, 993–995.
- Wang, J.L., Duboc, C., Wu, Q., Ochi, T., Liang, S., Tsutakawa, S.E., Lees-Miller, S.P., Nadal, M., Tainer, J.A., Blundell, T.L., and Strick, T.R. (2018). Dissection of DNA double-strand-break repair using novel single-molecule forceps. *Nat. Struct. Mol. Biol.* 25, 482–487.
- Waters, C.A., Strande, N.T., Wyatt, D.W., Pryor, J.M., and Ramsden, D.A. (2014a). Nonhomologous end joining: a good solution for bad ends. *DNA Repair (Amst.)* 17, 39–51.
- Waters, C.A., Strande, N.T., Pryor, J.M., Strom, C.N., Mieczkowski, P., Burkhalter, M.D., Oh, S., Qaqish, B.F., Moore, D.T., Hendrickson, E.A., and Ramsden, D.A. (2014b). The fidelity of the ligation step determines how ends are resolved during nonhomologous end joining. *Nat. Commun.* 5, 4286.
- Westmoreland, J.W., and Resnick, M.A. (2013). Coincident resection at both ends of random, γ -induced double-strand breaks requires MRX (MRN), Sae2 (Ctp1), and Mre11-nuclease. *PLoS Genet.* 9, e1003420.
- Williams, R.S., Moncalian, G., Williams, J.S., Yamada, Y., Limbo, O., Shin, D.S., Grocock, L.M., Cahill, D., Hitomi, C., Guenther, G., et al. (2008). Mre11 dimers coordinate DNA end bridging and nuclease processing in double-strand-break repair. *Cell* 135, 97–109.
- Xing, M., Yang, M., Huo, W., Feng, F., Wei, L., Jiang, W., Ning, S., Yan, Z., Li, W., Wang, Q., et al. (2015). Interactome analysis identifies a new paralogue of XRCC4 in non-homologous end joining DNA repair pathway. *Nat. Commun.* 6, 6233.
- Yang, S.W., Burgin, A.B., Jr., Huizenga, B.N., Robertson, C.A., Yao, K.C., and Nash, H.A. (1996). A eukaryotic enzyme that can disjoin dead-end covalent complexes between DNA and type I topoisomerases. *Proc. Natl. Acad. Sci. USA* 93, 11534–11539.
- Yoo, S., and Dynan, W.S. (1999). Geometry of a complex formed by double strand break repair proteins at a single DNA end: recruitment of DNA-PKcs induces inward translocation of Ku protein. *Nucleic Acids Res.* 27, 4679–4686.
- Zhao, B., Watanabe, G., Morten, M.J., Reid, D.A., Rothenberg, E., and Lieber, M.R. (2019). The essential elements for the noncovalent association of two DNA ends during NHEJ synthesis. *Nat. Commun.* 10, 3588.
- Zhu, M., Zhao, H., Limbo, O., and Russell, P. (2018). Mre11 complex links sister chromatids to promote repair of a collapsed replication fork. *Proc. Natl. Acad. Sci. USA* 115, 8793–8798.

STAR★METHODS

KEY RESOURCES TABLE

| REAGENT or RESOURCE | SOURCE | IDENTIFIER |
|--|--|------------------------------------|
| Antibodies | | |
| Rabbit α -Ku80 (<i>Xenopus</i>) | Graham et al., 2016 | N/A |
| Rabbit α -XLF (<i>Xenopus</i>) | Graham et al., 2016 | N/A |
| Rabbit α -XRCC4 (<i>Xenopus</i>) | Graham et al., 2016 | N/A |
| Rabbit α -DNA-PKcs (<i>Xenopus</i>) | Graham et al., 2016 | N/A |
| Rabbit α -ORC2 (<i>Xenopus</i>) | Walter and Newport, 1997 | N/A |
| Rabbit α -Tdp1 (<i>Xenopus</i>) | This study | N/A |
| Rabbit α -Artemis (<i>Xenopus</i>) | This study | N/A |
| Rabbit α -PNKP (<i>Xenopus</i>) | This study | N/A |
| Rabbit α -pol λ (<i>Xenopus</i>) | This study | N/A |
| Rabbit α -pol μ (<i>Xenopus</i>) | This study | N/A |
| Goat α -rabbit IgG, horseradish peroxidase-conjugated | Jackson ImmunoResearch | Cat# 111-035-003; RRID: AB_2313567 |
| Bacterial and Virus Strains | | |
| Rosetta 2(DE3) <i>E. coli</i> | Novagen | Cat# 71400 |
| Chemicals, Peptides, and Recombinant Proteins | | |
| Sulfo-Cyanine3 NHS ester | Lumiprobe | Cat# 11320 |
| Sulfo-Cyanine5 NHS ester | Lumiprobe | Cat# 13320 |
| Cy3B NHS ester | GE Healthcare | Cat# PA63101 |
| ATTO 647N NHS ester | ATTO-TEC | Cat# AD 647-31 |
| NU7441 | R&D Systems, Inc. | Cat# 3712 |
| γ - ³² P-ATP | Perkin Elmer | Cat# BLU502A250UC |
| Amino-11-dUTP | Lumiprobe | Cat# 26040 |
| BHQ-10 succinimidyl ester | Biosearch Technologies | Cat# BHQ-10S-5 |
| <i>Xenopus laevis</i> Lig4-XRCC4 | This study | N/A |
| <i>Xenopus laevis</i> PNKP | This study | N/A |
| <i>Xenopus laevis</i> pol λ | This study | N/A |
| <i>Xenopus laevis</i> pol μ | This study | N/A |
| <i>Xenopus laevis</i> Tdp1 | This study | N/A |
| Protein A Sepharose Fast Flow | GE Healthcare | Cat# 17127903 |
| AminoLink Coupling Resin | Thermo Scientific | Cat# 20382 |
| Nocodazole | Sigma | Cat# M1404 |
| mPEG-SVA, MW 5,000 | Laysan Bio | Cat# MPEG-SVA-5K-1g |
| Biotin-PEG-SVA, MW 5,000 | Laysan Bio | Cat# Bio-PEG-SVA-5k-100mg |
| Streptavidin | Sigma | Cat# S4762 |
| Protocatechuic acid | Sigma | Cat# 37580 |
| Protocatechuate 3,4-dioxygenase | Sigma | Cat# P8279 |
| Trolox | Sigma | Cat# 238813 |
| Streptavidin-coupled magnetic Dynabeads M-280 | Invitrogen | Cat# 11206D |
| Experimental Models: Organisms/Strains | | |
| <i>Xenopus laevis</i> , adult female | Nasco | Cat# LM00535 |
| Oligonucleotides | | |
| Please see Table S1 . | N/A | N/A |

(Continued on next page)

Continued

| REAGENT or RESOURCE | SOURCE | IDENTIFIER |
|---|---------------------------|---|
| Recombinant DNA | | |
| pBMS6 | This study | N/A |
| pBMS10 (PNKP expression) | This study | N/A |
| pBMS49 (L4 ^{WT} X4 expression) | This study | N/A |
| pBMS50 (L4 ^{ci} X4 expression) | This study | N/A |
| pBMS14 (pol μ expression) | This study | N/A |
| pBMS25 (pol λ expression) | This study | N/A |
| pBMS60 (Tdp1 expression) | This study | N/A |
| Software and Algorithms | | |
| MATLAB | Mathworks | https://www.mathworks.com/products/matlab.html |
| HCIImage Live | Hamamatsu | https://hciimage.com/hciimage-overview/hciimage-live/ |
| iSMS | Preus et al., 2015 | http://inano.au.dk/about/research-groups/single-molecule-biophotonics-group-victoria-birkedal/software/ |
| ebFRET | van de Meent et al., 2014 | http://ebfret.github.io/ |
| ImageJ | NIH | https://imagej.nih.gov/ij/index.html |
| Other | | |
| High Speed Supernatant (HSS) | Lebofsky et al., 2009 | N/A |

LEAD CONTACT AND MATERIALS AVAILABILITY

Further information and requests for resources and reagents should be directed to and will be fulfilled by the Lead Contact, Joseph Loparo (Joseph_Loparo@hms.harvard.edu). Plasmids generated in this study are available without restriction. Custom antibodies generated in this study are available as crude serum, although the quantities distributed may be limited by our need to maintain a stock.

EXPERIMENTAL MODEL AND SUBJECT DETAILS

Egg extracts were prepared using adult female *Xenopus laevis* (Nasco Cat# LM00535). Frogs were cared for by the Center for Animal Resources and Comparative Medicine at Harvard Medical School (AAALAC accredited). Work performed for this study was in accordance with the rules and regulations set by AAALAC. The Institutional Animal Care and Use Committee (IACUC) of Harvard Medical School approved the work.

METHOD DETAILS

Egg extract preparation

High-speed supernatant (HSS) of egg cytosol was prepared as described (Lebofsky et al., 2009).

Preparation of DNA substrates

A schematic of DNA substrate preparation is depicted in Figure S1A, and oligonucleotides are listed in Table S1. pBMS6, a derivative of pBlueScript, was linearized with SphI and AatII (New England Biolabs). The resulting 2977 bp fragment was separated on a 1x TBE agarose gel and recovered by electroelution and ethanol precipitation. Duplex oligonucleotide adapters (Integrated DNA Technologies, Inc.) were ligated to each side of this backbone fragment to generate the described DNA substrates.

To generate duplex adapters, oligonucleotide stocks (10 μ M) in annealing buffer (10 mM Tris, pH 8.0, 50 mM NaCl, 1 mM EDTA) were combined in equal volumes and annealed by heating to 95°C for 2 min then slowly cooling to room temperature in 1°C steps lasting 60 s. One duplex adaptor (oligos 1-2 in Figure S1A) contained an overhang complementary to that generated by SphI; similarly, the second duplex adaptor (oligos 3-4) contained an overhang complementary to that generated by AatII. Oligonucleotides (1) and (4) were phosphorylated with T4 PNK (New England Biolabs) to allow ligation to the backbone fragment. Oligonucleotides (2) and (3) were not phosphorylated at the annealing stage.

To generate most radiolabeled DNA substrates, γ - ^{32}P -ATP (Perkin Elmer) was used to phosphorylate oligonucleotide (1). To label the opposite strand (e.g., Figure 2C), the backbone fragment was treated with Shrimp Alkaline Phosphatase (NEB) prior to phosphorylation with γ - ^{32}P -ATP. In both cases, ends were first phosphorylated for 30 min with γ - ^{32}P -ATP, and subsequently 50 μM cold ATP was added and the reaction was allowed to proceed a further 15 min to ensure maximal phosphorylation.

Duplex adapters (250 nM) were ligated to the backbone fragment (25 nM) with T4 DNA ligase (New England Biolabs). The desired ~ 3 kb product was separated on a 1x TBE agarose gel and recovered by electroelution and ethanol precipitation (fluorescent DNA substrates) or with the QIAquick gel extraction kit (QIAGEN).

Single-molecule DNA substrates were generated in the same way using fluorescently labeled oligos (prepared as described below). Subsequently, the recovered DNA was treated with Nt.BbvCI (New England Biolabs) to introduce two nicks on the same strand near the middle of the molecule, thereby allowing removal of a 25-mer oligonucleotide. A 10-fold molar excess of an internally biotinylated, 5'-phosphorylated oligonucleotide with the same sequence was then added to the digestion mixture, and the mixture was subjected to the same annealing protocol as above, allowing insertion of the biotinylated oligo. The mixture was then treated with T4 DNA ligase, separated on a 1x TBE agarose gel, and the appropriate band was recovered by electroelution and ethanol precipitation.

Finally, all substrates, with the exception of that shown in Figures 2C, S1H (lanes 7–12), S2D, and S6E, were phosphorylated with T4 PNK prior to use.

Preparation of fluorescently-labeled oligonucleotides

Amino-modified synthetic oligonucleotides (see Table S1) were reacted with NHS-ester fluorophore derivatives. A typical labeling reaction contained 46 μL labeling buffer (100 mM sodium tetraborate, pH 8.5), 2 μL amino-modified oligo (25 mg/mL stock in water), and 2 μL NHS-ester fluorophore (50 mg/mL stock in DMSO). The reaction was allowed to proceed overnight at room temperature in the dark. The mixture was ethanol precipitated to remove excess fluorophore. The pellet was resuspended in ~ 10 μL Gel Loading Buffer II (Invitrogen) and subjected to denaturing PAGE electrophoresis on a 20% Urea-PAGE gel. The band corresponding to the labeled oligo was excised and crushed by centrifugation through a 1.7 mL microcentrifuge tube with a hole in the bottom made with an 18-gauge needle. 500 μL TE buffer (10 mM Tris, pH 8.0, 0.1 mM EDTA) was added to the crushed gel slice, and the mixture was frozen in liquid nitrogen, rapidly thawed in warm water, and rotated overnight at room temperature in the dark. The solution was collected, and the labeled oligo was recovered by ethanol precipitation.

Preparation of dUTP^Q

dUTP^Q (Figure S3B) was prepared by conjugating Amino-11-dUTP (Lumiprobe) to BHQ-10 succinimidyl ester (Biosearch Technologies). In a typical reaction, 2 μL 50 mM Amino-11-dUTP and 2.5 μL 50 mM BHQ-10 succinimidyl ester were mixed with 45.5 μL 100 mM sodium tetraborate, pH 8.5, and the reaction was allowed to proceed overnight at room temperature in the dark. The mixture was separated on a HiTrapQ column (GE Healthcare) using an AKTA pure chromatography system (GE Healthcare). The mixture was diluted 10-fold in solvent A (10% acetonitrile in water) and loaded onto the column, followed by a gradient of 0%–100% solvent B (3 M LiCl) over 20 column volumes. The elution profile of the mixture showed a single additional peak with absorbance at 516 nm relative to the elution profiles of Amino-11-dUTP and BHQ-10 succinimidyl ester alone. Fractions corresponding to this peak were pooled and added to 30 volumes ice-cold acetone to precipitate dUTP^Q, which was collected by centrifugation, washed with cold acetone, and resuspended in 10 mM Tris, pH 8.0.

Protein expression and purification

Ku70/80 and XLF were gifts from T. Graham and were purified as described (Graham et al., 2016). A Coomassie-stained SDS-PAGE gel of recombinantly-purified proteins is shown in Figure S11.

General procedure for purification of H₆-SUMO-tagged proteins:

Cells were grown at 37°C to O.D. 0.5–0.7 in LB broth (typically 2 L) and moved to 18°C for overnight (~ 16 hr) induction with 1 mM IPTG. Cells were harvested by centrifugation and resuspended in ice-cold Ni-NTA lysis buffer (20 mM HEPES, pH 7.5, 400 mM NaCl, 20 mM imidazole, 10% glycerol, 1 mM DTT; 20 mL per L of culture). Resuspended cells were lysed by sonication in the presence of cOmplete Protease Inhibitor Cocktail, EDTA-free (Roche). Lysates were clarified by centrifugation at 20,000 *rcf*. for 60 min, and the supernatant was added to Ni-NTA agarose resin (0.5 mL bed volume per liter of cell culture; QIAGEN) equilibrated in Ni-NTA lysis buffer and agitated by rocking at 4°C for 60 min. Resin was collected by centrifugation, washed once with 10 mL Ni-NTA lysis buffer, resuspended in ~ 10 mL Ni-NTA lysis buffer and applied to a polypropylene gravity flow column. The resin was washed twice with 10 mL Ni-NTA lysis buffer, and bound proteins were eluted with 1 mL fractions of Ni-NTA elution buffer (Ni-NTA lysis buffer with 250 mM imidazole). Fractions containing protein (determined by Bradford assay; Biorad) were concentrated using a 10,000 MWCO centrifugal filter (Amicon) and desalted using a PD-10 column (GE Healthcare) equilibrated in Ulp1 cleavage buffer (20 mM HEPES, pH 7.5, 150 mM NaCl, 10% glycerol, 1 mM DTT) according to the manufacturer's instructions. The H₆-SUMO tag was removed by treatment with H₆-tagged Ulp1 protease (~ 30 $\mu\text{g}/\text{mL}$ final concentration) as described for each individual protein below. Imidazole (20 mM final concentration) was added to the reaction mixture, which was then passed over a 0.5 mL Ni-NTA agarose column equilibrated in Ulp1 reaction buffer supplemented with 20 mM imidazole. The flow-through was collected, including a 1 mL wash to collect protein remaining in the void volume, and subjected to further purification steps as indicated below for each protein.

Lig4-XRCC4

X. laevis Lig4 and XRCC4 coding sequences (Thermo Scientific ClonID 6635763 and 6957895) were subcloned into the pETDuet-1 vector (Novagen), and an N-terminal H₆-SUMO tag was introduced to Lig4. The resulting plasmid (pBMS49 for wild-type Lig4; pBMS50 for the K278R catalytically-inactive mutant) was transformed into Rosetta II (DE3) cells (Novagen), and overexpression and initial purification were performed as described in “General Procedure for Purification of H₆-SUMO-Tagged Proteins,” with Ulp1 cleavage carried out at room temperature for 2 hr. The flowthrough following clean-up of the Ulp1 cleavage mixture was diluted three-fold with dilution buffer (20 mM HEPES, pH 7.5, 10% glycerol, 1 mM DTT) and purified by anion exchange chromatography (MonoQ 5/50GL, GE Healthcare) on an AKTA pure chromatography system (GE Healthcare). Sample was applied to the column, washed with buffer A (20 mM HEPES, pH 7.5, 50 mM NaCl, 10% glycerol, 1 mM DTT), and eluted with a gradient of 0%–60% buffer B (20 mM HEPES, pH 7.5, 1 M NaCl, 10% glycerol, 1 mM DTT) over 20 column volumes. Fractions were analyzed by SDS-PAGE, and those containing Lig4-XRCC4 were pooled and concentrated to ~0.5 mL using a 10,000 MWCO centrifugal filter. The sample was applied to a Superdex 200 Increase column (GE Healthcare) equilibrated in Ulp1 cleavage buffer. Fractions were analyzed by SDS-PAGE, pooled, concentrated, flash-frozen in liquid nitrogen, and stored at –80°C until use.

PNKP

The *X. laevis* PNKP coding sequence was amplified from egg cDNA (gift of T. Graham) and subcloned into an N-terminal H₆-SUMO tag expression vector. The resulting plasmid (pBMS10) was transformed into Rosetta II (DE3) cells, and overexpression and initial purification were performed as described in “General Procedure for Purification of H₆-SUMO-Tagged Proteins,” except Ulp1 cleavage buffer was supplemented with additional NaCl (300 mM total). Ulp1 cleavage was carried out at 30°C for 4 hr, and the mixture was centrifuged at 20,000 *rcf.* for 15 min to remove precipitates. The flowthrough following clean-up of the Ulp1 cleavage mixture was diluted six-fold with dilution buffer (20 mM HEPES, pH 7.5, 10% glycerol, 1 mM DTT) and purified by cation exchange chromatography (MonoS 5/50 GL, GE Healthcare) on an AKTA pure chromatography system (buffer A: 20 mM HEPES, pH 7.5, 50 mM NaCl, 10% glycerol, 1 mM DTT; buffer B: buffer A with 1 M NaCl). Sample was applied to the column, washed with 15% buffer B, and eluted with a gradient of 15%–40% buffer B over 20 column volumes. Fractions were analyzed by SDS-PAGE, and those containing PNKP were pooled and concentrated to ~0.5 mL using a 10,000 MWCO centrifugal filter. The sample was applied to a Superdex 200 Increase column (GE Healthcare) equilibrated in Ulp1 cleavage buffer. Fractions were analyzed by SDS-PAGE, pooled, concentrated, flash-frozen in liquid nitrogen, and stored at –80°C until use.

pol λ and pol μ

X. laevis pol λ and pol μ coding sequences were amplified from egg cDNA and subcloned into an N-terminal H₆-SUMO tag expression vector. The resulting plasmids (H₆-SUMO-pol λ, pBMS25; (H₆-SUMO-pol μ, pBMS14) were transformed into Rosetta II (DE3) cells, and overexpression and initial purification were performed as described in “General Procedure for Purification of H₆-SUMO-Tagged Proteins,” with Ulp1 cleavage carried out at room temperature for 90 min. The flowthrough following clean-up of the Ulp1 cleavage mixture was applied to a Superdex 200 Increase column equilibrated in Ulp1 cleavage buffer. Fractions were analyzed by SDS-PAGE, pooled, concentrated, flash-frozen in liquid nitrogen, and stored at –80°C until use.

Tdp1

The *X. laevis* Tdp1 coding sequence (XGC ClonID 6638604; Dharmacon) was subcloned into N-terminal H₆-SUMO tag expression vector. The resulting plasmid (pBMS60) was transformed into Rosetta II (DE3) cells, and overexpression and initial purification were performed as described in “General Procedure for Purification of H₆-SUMO-Tagged Proteins” with the following modification: Ulp1 was added to the initial Ni-NTA eluate, and the mixture was dialyzed using 12–14 kDa MWCO dialysis tubing (Spectra/Por) against 1 L Ulp1 cleavage buffer overnight at 4°C. The flowthrough following clean-up of the Ulp1 cleavage mixture was diluted three-fold with dilution buffer (20 mM HEPES, pH 7.5, 10% glycerol, 1 mM DTT) and purified by cation exchange chromatography (MonoS 5/50 GL, GE Healthcare) on an AKTA pure chromatography system (GE Healthcare). Sample was applied to the column, washed with buffer A (20 mM HEPES, pH 7.5, 50 mM NaCl, 10% glycerol, 1 mM DTT), and eluted with a gradient of 0%–50% buffer B (20 mM HEPES, pH 7.5, 1 M NaCl, 10% glycerol, 1 mM DTT) over 20 column volumes. Fractions were analyzed by SDS-PAGE, and those containing Tdp1 were pooled and concentrated to ~0.5 mL by binding to a small volume of SP Sepharose resin (GE Healthcare) and elution with 50% buffer B. The sample was applied to a Superdex 200 Increase column (GE Healthcare) equilibrated in Ulp1 cleavage buffer. Fractions were analyzed by SDS-PAGE, pooled, concentrated with SP Sepharose resin as above, flash-frozen in liquid nitrogen, and stored at –80°C until use.

Antibodies and immunodepletion

Rabbit polyclonal antibodies raised against the following *X. laevis* proteins were previously described: Ku80 (Graham et al., 2016), XLF (Graham et al., 2016), XRCC4 (Graham et al., 2016), DNA-PKcs (Graham et al., 2016), and ORC2 (Walter and Newport, 1997). Rabbit polyclonal antibodies were raised against full-length recombinant *X. laevis* PNKP, pol λ, and pol μ (purified as described above) by Pocono Rabbit Farm & Laboratory, Inc. Rabbit polyclonal antibody against *X. laevis* Artemis was raised against the peptide CKLQHVVYKRLAMGDNVL by New England Peptide. Rabbit polyclonal antibody against *X. laevis* Tdp1 was raised against the peptide MDRTSASQSQSYGK by New England Peptide. Rabbit polyclonal antibody against *X. laevis* Mre11 was raised against the peptide CDDEEDFDPFKKSGPSRRGR by Bethyl Laboratories.

DNA-PKcs, PNKP, pol λ, and pol μ antibodies were affinity purified from rabbit serum by coupling each recombinant protein antigen to AminoLink Coupling Resin (Thermo Scientific) and following manufacturer’s instructions for IgG purification.

Unless noted otherwise below, all immunodepletions were carried out by the same procedure. 3 volumes of 1 mg/mL affinity-purified antibody (10 volumes for Mre11 antibody; 20 volumes for DNA-PKcs antibody) was gently rotated with 1 volume Protein A Sepharose beads (GE Healthcare) overnight at 4°C or 1 hour at room temperature. Beads were washed extensively with ELBS (2.5 mM MgCl₂, 50 mM KCl, 10 mM HEPES, pH 7.7, 0.25 M sucrose), and five volumes of egg extract containing 7.5 ng/μL nocodazole were immunodepleted by three rounds of gentle rotation with one volume of antibody-bound beads for 60 min at 4°C. Immunodepleted extracts were either used immediately or flash-frozen in liquid nitrogen. For co-immunodepletions, 3 volumes of each 1 mg/mL affinity-purified antibody (10 volumes for Mre11 antibody) was added to 1 volume Protein A Sepharose beads. Mock depletions were performed using IgG purified from rabbit pre-immune serum using Protein A Sepharose beads.

λ protein phosphatase treatment of endogenous Tdp1 (Figure S1E(ii)) was performed in the following manner. 20 μL extract was subjected to a single round of Tdp1 immunodepletion as described above. Beads were washed twice with ELBS and suspended in 20 μL PMP buffer supplemented with 1 mM MnCl₂ (NEB). 200 units λ protein phosphatase (NEB) was added to 10 μL of the suspension, and the reaction was incubated at 30°C for 30 min before addition of one volume 2x reducing Laemmli sample buffer and immunoblotting as described below.

Immunoblotting

Samples were resolved on Mini-PROTEAN precast gels (Bio-Rad) and transferred to PVDF membranes (Perkin Elmer). Membranes were blocked in 5% nonfat milk in 1x PBST for 60 min at room temperature, then incubated with antibody diluted 1:2000 in 1x PBST containing 1% BSA for 60 min at room temperature or overnight at 4°C. After extensive washing in 1x PBST at room temperature, the membranes were incubated with goat anti-rabbit IgG horseradish peroxidase-conjugated antibody (Jackson ImmunoResearch) diluted 1:20,000 in 5% nonfat milk in 1x PBST for 45 min at room temperature. Membranes were washed extensively in 1x PBST, incubated for ~60 s with HyGLO chemiluminescent HRP antibody detection reagent (Denville), and imaged using an Amersham Imager 600 (GE Healthcare).

Ensemble NHEJ assays

Ensemble NHEJ assays were conducted at room temperature. Egg extracts were supplemented with the following (final concentration indicated in parentheses): nocodazole (7.5 ng/μL) if nocodazole had not been added during prior immunodepletion; pBMS6 (10 ng/μL); ATP (3 mM); phosphocreatine (15 mM); and creatine phosphokinase (0.01 mg/mL; Sigma). Joining reactions were initiated by addition of 5 ng/μL radiolabeled linear DNA substrate (final concentration, prepared as described above).

For analysis by agarose gel electrophoresis, samples were withdrawn at the indicated times and mixed with a 2.5 volumes agarose stop solution (80 mM Tris, pH 8.0, 8 mM EDTA, 0.13% phosphoric acid, 10% Ficoll, 5% SDS, 0.2% bromophenol blue). Samples were treated with Proteinase K (1.4 mg/mL final concentration) for 60 min at 37°C or room temperature overnight, and products were separated by electrophoresis on a 1x TBE 0.8% agarose gel. Gels were dried under vacuum on a HyBondXL nylon membrane (GE Healthcare) and exposed to a storage phosphor screen, which was imaged with a Typhoon FLA 7000 imager (GE Healthcare).

For analysis by denaturing urea-PAGE, samples were withdrawn at the indicated times and mixed with 10 volumes extraction stop solution (100 mM Tris, pH 8.0, 25 mM EDTA, 0.5% SDS). Samples were treated with RNase A (0.2 mg/mL final concentration) for 30 min at 37°C and then treated with Proteinase K (0.67 mg/mL final concentration) for 60 min at 37°C or room temperature overnight. Samples were phenol-chloroform extracted, ethanol precipitated, resuspended, and simultaneously digested with SacI and KpnI (NEB). Digestion was stopped by addition of 1 volume Gel Loading Buffer II (Invitrogen). A denaturing sequencing gel (6% acrylamide/bis-acrylamide [5% crosslinker], 7 M urea, 40% formamide) was pre-run on a LABREPCO Model S2 apparatus with 0.8x glycerol tolerant gel buffer (20x stock: 1.78M Tris, 0.57 M taurine, 0.01 M EDTA) for 60 min before loading samples, which were heated to 95°C for 2 min and rapidly cooled on ice just prior to loading. Following electrophoresis, the gel was fixed in 20% methanol/10% acetic acid for ~45 min, transferred to Whatman 3 MM Chr filter paper, dried under vacuum, and exposed to a storage phosphor screen, which was imaged with a Typhoon FLA 7000 imager. Sequencing ladders were generated using the Thermo Sequenase Cycle Sequencing kit (Affymetrix) according to the manufacturer's instructions.

Deep sequencing of NHEJ products

Joining reactions were carried out as described above for 90 min. Products were separated on a 1x TBE, 0.8% agarose gel and stained with SYBR Gold (Invitrogen). The band corresponding to closed-circular plasmid was excised and extracted with the QIAquick gel extraction kit (QIAGEN). A second independent replicate was performed, and the recovered DNA was pooled. This material served as the template for amplification by PCR prior to next-generation sequencing. For each sample, a ~200 bp amplicon was generated from 1 × 10⁶ template molecules by PCR in 22 cycles using Phusion polymerase (NEB), purified with the QIAquick gel extraction kit, and submitted to Genewiz for the Amplicon-EZ service (paired-end Illumina sequencing) and analysis. Reads were aligned using a 40 bp target sequence centered at the break site and compared to the reference sequence corresponding to direct joining. Two control templates were amplified in parallel: (1) a template of known sequence, to control for errors in amplification and library preparation, and (2) a mixture of three templates in a defined ratio of 48 ("WT"): 1 (1 bp substitution): 1 (12 bp deletion), to ensure relatively rare sequences were recovered. Control (1) returned 98.5% of reads with the expected sequence. Control (2) re-

turned the expected reads in a ratio of 43:1:2. Deviation from the expected 48:1:1 ratio is likely due to slight amplification bias toward the shorter amplicon and heterogeneity in the template, which in this case was synthetic double-stranded DNA fragments. The analysis results for all samples are reported in Data S1.

Single-molecule microscope and chamber preparation

Samples were imaged with a through-objective TIRF microscope built around an Olympus IX-71 inverted microscope body. 532-nm, and 641-nm laser beams (Coherent Sapphire 532, and Cube 641, respectively) were expanded, combined with dichroic mirrors, expanded again, and focused on the rear focal plane of an oil-immersion objective (Olympus UPlanSApo, 100 \times ; NA, 1.40). The focusing lens was placed on a vertical translation stage to permit manual adjustment of the TIRF angle. Emission light was separated from excitation light with a multipass dichroic mirror, and laser lines were further attenuated with a StopLine 488/532/635 notch filter (Semrock). A home-built beamsplitter (Graham et al., 2017) was used to separate Cy3 emission from Cy5 emission; these two channels were imaged on separate halves of an electron-multiplying charge-coupled device camera (Hamamatsu, ImageEM 9100-13), which was operated at maximum EM gain. An automated microstage (Mad City Labs) was used to position the sample and move between fields of view.

Microfluidic chambers were constructed in the following manner: a Dremel tool with a diamond-tipped rotary bit was used to drill two holes 10 mm apart in a glass microscope slide; PE20 tubing was inserted into one hole and PE60 tubing into the other (Intra-med), and the tubing was cut flush on one side of the slide and fixed in place with epoxy (Devcon) on the other; double-sided SecureSeal Adhesive Sheet (Grace Bio-Labs), into which a 1.5 \times 12 mm channel had been cut, was placed on the non-tubing side of the slide, aligning the channel with the holes in the slide. A glass coverslip, functionalized with a mixture of methoxypolyethylene glycol-succinimidyl valerate, MW 5,000 (mPEG-SVA-5000; Laysan Bio, Inc.) and biotin-methoxypolyethylene glycol-succinimidyl valerate, MW 5,000 (biotin-PEG-SVA-5000; Laysan Bio, Inc.) as previously described (Graham et al., 2017), was then placed on the second side of the adhesive sheet, and the edges of the coverslip were sealed with epoxy.

Solutions were drawn into the chamber by attaching a 1 mL syringe to the PE60 tubing. Flow cells were incubated with 1 mg/mL streptavidin (Sigma) in PBS for \sim 2 min. Unbound streptavidin was washed out with ELB150 (2.5 mM MgCl₂, 150 mM KCl, 10 mM HEPES, pH 7.7) and biotinylated DNA substrates were incubated in the channel at a concentration yielding appropriate surface density (typically \sim 1 nM, diluted in ELB150). Unbound DNA was washed out with ELB150 and experiments were performed as indicated below.

Analysis of single-molecule data

Analysis of single-molecule experiments in egg extracts was performed essentially as described (Graham et al., 2016, 2017) using custom MATLAB scripts, with modifications as noted below. Fluorescence intensities were corrected for donor bleedthrough in the acceptor channel, direct acceptor excitation by the 532 nm laser, and differences in donor/acceptor quantum yield and detection efficiency as described (Graham et al., 2016).

Single-molecule assay for polymerase activity

To remove endogenous dNTPs, 30 μ L egg extract was applied to and eluted from a Micro Bio-Spin 6 column (Bio-Rad) equilibrated in ELB150. The buffer-exchanged extract was supplemented with the following (final concentrations in parentheses): nocodazole (7.5 ng/ μ L) if nocodazole had not been added during prior immunodepletion; intact pBMS6 (10 ng/ μ L); SphI/AatII-digested pBMS6 (2.5 ng/ μ L); ATP (3 mM); phosphocreatine (15 mM); creatine phosphokinase (0.01 mg/mL; Sigma); dATP, dCTP, dGTP (50 μ M each); dUTPQ or dTTP, as indicated (50 μ M); protocatechuic acid (PCA; 5 mM; Sigma); protocatechuic 3,4-dioxygenase (PCD; 0.1 μ M; Sigma); and Trolox (6-Hydroxy-2,5,7,8-tetramethylchromane-2-carboxylic acid; 1 mM; Sigma). PCA and PCD constitute an oxygen-scavenging system and Trolox functions as a triplet-state quencher to improve fluorophore performance. A recent study concluded that the PCA/PCD oxygen scavenging system inhibits DNA-PKcs kinase activity (Zhao et al., 2019). We note that the concentrations of PCA/PCD used in our study allow for robust end joining in egg extracts, and we observe strong effects upon inhibition of DNA-PKcs with NU7441 when PCA/PCD is also present (Figures S2Aii and S4C). We therefore conclude that DNA-PKcs is functional under the conditions used in our study.

The biotinylated, fluorescent DNA substrate, generated as described above using oligonucleotides listed in Table S1, was immobilized on a glass coverslip in a microfluidic chamber. Extract was introduced to the chamber and images were taken continuously at a rate of 1 frame/s for 900 s, alternating between two frames of 532 nm excitation and one frame of 641 nm excitation. Surface laser power density was measured using a Coherent FieldMate power meter with an OP-2 VIS detector (532 nm: 2 mW/cm²; 641 nm: 0.6 mW/cm²).

In the experiments shown in Figures 4 and S4, peak selection was performed with a slightly modified protocol: 2D Gaussian fitting was performed on images from both channels, as well as the same images rotated 45 degrees, and spots were accepted for analysis only if the ellipticity of all fits (ratio of major to minor axis width) were below a specified cutoff. The same images were rotated 45 degrees and subjected to the same ellipticity analysis to exclude spots distorted in a diagonal direction. Additionally, peaks with donor and acceptor centroids displaced by more than 1.25 pixels between channels were rejected. Custom MATLAB scripts were used to automatically identify donor and acceptor photobleaching, FRET transitions, and donor quenching. Trajectories were truncated due to donor photobleaching when, during donor excitation, donor and acceptor intensity fell and remained below a threshold set at 25%

of initial donor intensity. Trajectories were truncated due to acceptor photobleaching when, during acceptor excitation, acceptor intensity fell and remained below a threshold set at 25% of initial acceptor intensity. FRET transitions were detected by locating peaks above a set threshold in the first derivative (MATLAB gradient function) of the smoothed FRET signal (MATLAB smooth function). Trajectories of non-photobleached molecules were truncated due to donor quenching when the average donor intensity in a 6-frame window fell below a threshold set at 40% of the average intensity of the preceding 3 frames without a concomitant FRET transition. Quenching frequency in Figure 4 was calculated by dividing the number of quenching events by the total observation time prior to censoring by quenching, donor or acceptor photobleaching, or end of experiment. Observation times were identical for all experiments (900 s). Survival plots in Figure S4 were generated in MATLAB using (1-ecdf) accounting for right-censoring due to donor or acceptor photobleaching, substrate detachment, or end of experiment. Confidence bounds were calculated using Greenwood's formula. Survival plots in Figure 4E were similarly constructed, but also accounted for right-censoring upon a FRET transition.

For the single-color experiments shown in Figures S3D–S3L, the DNA substrate was generated by annealing the following oligos (with IDT modification codes) as described above:

CGTACCGCCC/iAmMC6T/ATGC (Cy3-labeled)
/5phos/GCAGGACGAAGCCGA /5Biosg/TCGGCTTCGTCTGCAGCATAGGGCGGTACG.

Peaks were selected and background-corrected intensities extracted using the iSMS MATLAB software package (Preus et al., 2015). A custom MATLAB script was used to truncate trajectories upon photobleaching and automatically identify quenching events, detected using a threshold set at 40% of the average intensity prior to the first flow-in step (see Figures S3E, S3I, and S3K). For Figures S3E, S3G, and S3H, intensities were extracted for molecules with a detected quenching event from the quenching event to the end of the trajectory, either due to photobleaching or experiment termination. These intensities were globally fitted to a two-state Hidden Markov Model using the ebFRET MATLAB software package (van de Meent et al., 2014) with default parameters. Cumulative probability plots in Figures S3G and S3H were generated from this fit using the MATLAB ecdf function with right-censoring and confidence bounds with Greenwood's formula.

Single-molecule assay for Tdp1 activity

For the experiments shown in Figures 5 and S5, extracts were depleted of Mre11 (and Tdp1 or Ku, as indicated) as described above. Extracts were supplemented with the following (final concentrations in parentheses): pBMS6 (10 ng/ μ L); un-labeled, linear DNA substrate generated as described above using oligonucleotides listed in Table S1 (2.5 ng/ μ L); ATP (3 mM); phosphocreatine (15 mM); creatine phosphokinase (0.01 mg/mL); PCA (5 mM); PCD (0.1 μ M); and Trolox (1 mM).

The biotinylated, fluorescent DNA substrate, generated as described above using oligonucleotides listed in Table S1, was immobilized on a glass coverslip in a microfluidic chamber. Extract was introduced to the chamber and 100 ms exposures were taken stroboscopically every 1 s. The stage was moved after every exposure in a square pattern, allowing imaging of 4 fields of view in one experiment. 532 nm (surface power density 2 mW/cm²) and 641 nm excitation (surface power density 1.5 mW/cm²) were alternated such that for each field of view two frames of 532 nm excitation and one frame of 641 nm excitation were recorded with each frame separated by 4 s.

Peak selection was slightly modified to reject peaks whose donor and acceptor centroids were displaced by more than 1 pixel and peaks whose initial intensity fell outside a set window characteristic of single molecules. Custom MATLAB scripts were used to automatically identify acceptor photobleaching, FRET transitions, and donor loss/photobleaching. Trajectories were truncated due to acceptor photobleaching when, during acceptor excitation, acceptor intensity fell and remained below a threshold set at 25% of initial acceptor intensity. FRET transitions were detected by locating peaks above a set threshold in the gradient of the smoothed FRET signal. Trajectories were truncated due to donor loss/photobleaching when, during acceptor excitation, the sum of donor and acceptor intensity fell and remained below a threshold set at 25% of initial donor intensity. Events in which donor and acceptor intensity fell below their respective thresholds simultaneously, likely due to detachment of the DNA molecule from the coverslip, were not scored as donor loss events. Donor loss frequency in Figure 5 was calculated by dividing the number of donor loss events by the total observation time prior to censoring by donor loss, acceptor photobleaching, or end of experiment. Observation times were identical for all experiments (1800 s). Survival plots in Figures 5E and S5 were generated in MATLAB using (1-ecdf) accounting for right-censoring due to acceptor photobleaching, substrate detachment, end of experiment, or transition to the other FRET state. Confidence bounds were calculated using Greenwood's formula.

DNA-pulldown and analysis of protein enrichment on DSBs

Substrate generation

A 1 kb long DNA fragment with biotin molecules attached to the 5' termini (dibiotin-DNA) was generated by PCR amplification using Q5 High-Fidelity Polymerase (NEB), with pAM075 as a template and the 5'-biotinylated primer pair oAM091/oAM092. Biotinylated DNA fragments were isolated by electroelution from a 1.0% 1x TBE-agarose gel, ethanol precipitated, and stored in TE buffer at –20°C.

DNA-bead generation

For each biological replicate, 40 μ L of streptavidin-coated magnetic beads (Sigma, Dynabeads M-280) were used. Beads were prepared with two washes of 180 μ L of 2x binding and wash buffer (2xBWB; 10 mM Tris, pH 7.4, 2 M NaCl, and 20 mM EDTA). In between washes, the beads were centrifuged for 30 s at 5000 rpm in a microfuge (Eppendorf 5418) and then placed on a magnetic rack. The magnetic beads were resuspended in 180 μ L of 1xBWB containing 30 nM dibiotin-DNA and incubated for 20 minutes on a rotisserie at 25°C. DNA-bound beads were washed twice with 180 μ L of 2xBWB, twice with 80 μ L of 1x Cutsmart buffer (NEB), and then resuspended in 80 μ L of 1x Cutsmart buffer. The DNA-bead suspension was then split in half to prepare plasmid and DSB samples. 1 μ L of Xmn I restriction enzyme (NEB) was added to the DSB sample and then both samples were incubated at 37°C for six hours. Xmn I was removed by three washes of 80 μ L 2xBWB. To reduce non-specific binding, the beads were washed with 80 μ L of egg lysis blocking buffer (ELB-block; 10 mM HEPES, pH 7.7, 50 mM KCl, 2.5 mM MgCl₂, 250 mM sucrose, 0.25 mg/mL BSA, 0.03% casein, and 0.02% Tween20). Then, DNA-beads were blocked in 80 μ L of ELB-block for 20 minutes on ice and resuspended in 50 μ L ELB-block.

Pulldown of NHEJ Factors

For each biological replicate, 125 μ L of HSS was freshly thawed in the presence of nocadazole at a final concentration of 7.5 ng/ μ L. To reduce non-specific binding of aggregates to the DNA beads, the HSS was centrifuged (14000 rpm, 10 min., 4°C) in a fixed angle microfuge (Eppendorf 5418). The HSS was then split into two 50 μ L samples and the DNA-PKcs inhibitor NU-7441 (R&D Systems, Inc.), stored as 4 mM stock in DMSO, was added to a final concentration of 100 μ M for the PKcs-i sample, while an equivalent volume of DMSO was added to the other sample. After a 5 minute incubation on ice, an ATP regeneration system (ARS) was added to ensure constant ATP levels. 30x ARS stock contained 65 mM ATP (Sigma), 650 mM phosphocreatine (Sigma), and 160 ng/mL creatine phosphokinase (Sigma) and was used at 1x final concentration. Circular pBluescript II was added to the DNA-bead samples to a final concentration of 30 ng/ μ L. NHEJ reactions were initiated by mixing 25 μ L of the DNA-bead sample with an equal volume of HSS and incubating for 15 minutes on a rotisserie at 25°C. To isolate DNA-beads and associated proteins, 48 μ L of the total reaction was layered over 180 μ L of ELB-cushion solution (10 mM HEPES, pH 7.7, 50 mM KCl, 2.5 mM MgCl₂, 500 mM sucrose) in a 5 X 44 mm micro centrifuge tube (Beckman Coulter) and sedimented by centrifugation (12000 rpm, 45 s., 4°C) in a horizontal rotor (Kompspin, Ku Prima-18R). The pelleted DNA-beads was then washed with 180 μ L of ELB-block and resuspended in 50 μ L of 1x reducing Laemmli sample buffer. Input samples for western blotting were prepared by diluting HSS 1:40 in 1x reducing Laemmli sample buffer.

Western Blotting

Samples were separated on a 4%–15% precast SDS-PAGE gel (BioRad) for 2 hours at 100 V and transferred to a PVDF membrane for 50 minutes at 85 V at 4°C. Membranes were blocked with 5% powdered nonfat milk dissolved in 1x PBST for 30 minutes and then incubated with primary antibody diluted in 1x PBST containing 2.5% BSA (OmniPur) for 12–16 h at 4°C. Primary antibodies were used at the following concentrations: α -Ku80 1:10000, α -Pol λ 1:2000, α -Pol μ 1:2000, α -PNKP 1:2500, α -TDP1 1:4000, and α -Orc2 1:10000. After extensive washing with 1x PBST, membranes were incubated with goat anti-rabbit-HRP (Jackson ImmunoResearch) secondary antibody diluted 1:10,000 or 1:20,000 in 5% powdered nonfat milk and 1x PBST for 1 hour at room temperature. Membranes were washed again with 1x PBST, incubated with HyGLO Quick Spray (Denville Scientific), and imaged on an Amersham Imager 600 (GE Healthcare).

QUANTIFICATION AND STATISTICAL ANALYSIS

All ensemble experiments were performed at least twice, with a representative result shown. Statistical details for single molecule experiments can be found in the figure legends and [Method Details](#). No statistical methods were used to predetermine sample size.

For DNA-pulldown experiments, western blots were quantified with ImageJ using ORC2 as a normalization reference. All pull-downs were performed as three independent experiments, and quantitative data are expressed as mean \pm standard deviation. Statistical analyses were performed using an unpaired Student's t test in Windows Excel 2013. P values \leq 0.05 were considered significant for all analyses.

DATA AND CODE AVAILABILITY

The single-molecule datasets and custom MATLAB analysis code are available from the corresponding author on request.